

Parity violating magnetization at neutrino pair emission using trivalent lanthanoid ions

H. Hara, A. Yoshimi, and M. Yoshimura

Research Institute for Interdisciplinary Science, Okayama University
Tsushima-naka 3-1-1 Kita-ku Okayama 700-8530 Japan

ABSTRACT

A new, indirect detection method of neutrino pairs $\nu\bar{\nu}$ using magnetization generated at triggered radiative emission of neutrino pair (RENP), $|e\rangle \rightarrow |g\rangle + \gamma + \nu\bar{\nu}$ (atomic de-transition from state $|e\rangle$ to state $|g\rangle$ accompanied by a photon γ), is investigated in order to determine unknown neutrino properties; Majorana/Dirac distinction and absolute neutrino masses. Magnetization associated with RENP events has parity violating component intrinsic to weak interaction enforced by crystal field effect in solids, and greatly helps background rejection of quantum electrodynamic (QED) origin even when these backgrounds are amplified. In proposed experiment we prepare a coherently excited body of trivalent lanthanoid ions, Er^{3+} (a best candidate ion so far found), doped in a transparent dielectric crystal. The magnetic moment $\mu\langle\vec{S}\cdot\vec{k}\rangle/k$ arising from generated electron spin \vec{S} parallel to trigger photon direction \vec{k}/k is parity odd, and is absent in QED processes. The generated magnetic field of order nano gauss or larger is stored in crystals long after pair emission event till spin relaxation time. An improved calculation method of coherent rate and angular distribution of magnetization is developed in order to incorporate finite size effect of crystal target beyond the infinite size limit in previous calculations.

Keywords neutrino pair emission, Majorana neutrino, absolute value of neutrino mass, parity violation, magnetization in lanthanoid doped crystals, crystal field effect, SQUID, macro-coherence, four level optical Bloch equation

1 Introduction

Neutrino oscillation experiments, despite their remarkable discovery and measurement of finite neutrino mass and mixing in interactions, cannot determine remaining important neutrino properties and physical parameters, Majorana/Dirac distinction and absolute neutrino masses. These are key ingredients to explain the matter anti-matter imbalance in cosmology and construct the unified theory of particle physics. We proposed more than ten years ago an idea to solve these issues by using atoms/ions of typical eV energy release much closer to expected neutrino masses instead of atomic nuclei of typical MeV energy release. A mechanism of rate enhancement is crucial for weak processes, and we initiated experiments that verify the principle of enhanced event rates in weak QED process [1]. The enhancement region extends to a whole body of excited target consisting of many atoms/ions within which macro-coherence prevails. The spatial region of macro-coherence for multiple particle emission is much larger than the coherence region of single photon emission in Dicke's super-radiance scheme [2], which is limited by wavelength $1/k = \lambda/2\pi$. Our achieved rate enhancement reaches of order 10^{18} close to expectation in QED two-photon emission from excited vibrational state of para-hydrogen [3].

The process we have considered for neutrino study is either radiative neutrino pair $\nu\bar{\nu}$ emission (RENP) $|e\rangle \rightarrow |g\rangle + \gamma + \nu\bar{\nu}$ stimulated by trigger laser, or Raman stimulated radiative neutrino pair emission (RANP) [4] in atomic de-excitation between two states, $|e\rangle \rightarrow |g\rangle$. One measures either dependence on signal (stimulated by trigger) photon energy or angular distribution to extract neutrino properties. A large number of target atoms/ions close to those in solid environment is required for realistic RENP experiments. We shall consider a special crystal in the present work; trivalent lanthanoid ion Er^{3+} of low concentration doped in host crystals, known to have narrow radiative widths.

A potentially serious problem against RENP detection is QED backgrounds. Measurement of parity odd quantity, as first discussed in [5], in triggered neutrino pair emission is of great use to distinguish the process involving weak interaction from purely QED (Quantum Electro Dynamic) processes, even if they are macro-coherently amplified. Random QED backgrounds that mimic parity violating effects are separated, since parity violating quantities in QED average to zero in statistically meaningful data. An interesting quantity of this nature in RENP is magnetization arising from magnetic moments parallel to the trigger photon direction generated at neutrino pair emission: the expectation value in the final state $|f\rangle$ in RENP, $g\mu_B \langle f | \vec{S} \cdot \hat{k} | f \rangle$, where \hat{k} is the unit vector along the signal photon momentum \vec{k} and \vec{S} is the electron spin operator to be multiplied by $g\mu_B$, the g -factor times Bohr magneton for magnetization. This quantity is parity odd and time reversal (T) even. The generated magnetization due to these magnetic moments persists in crystals till spin relaxation time, of order msec or even larger in appropriate trivalent lanthanoid ions doped in host crystals. Measurement of an accumulated bulk quantity such as magnetization gives more freedom in experiments than direct event detection that rarely occurs [6].

Parity odd quantity emerges from interference term of parity even and odd amplitudes in the weak hamiltonian H_W of neutrino pair emission. Writing in terms of the neutrino mixing matrix elements, $U_{ei}, i = 1, 2, 3, \nu_e = \sum_i U_{ei}\nu_i$, the weak hamiltonian density consists of two terms of different parities,

$$H_W = \frac{G_F}{\sqrt{2}} \sum_{ij} \bar{\nu}_i \gamma^\alpha (1 - \gamma_5) \nu_j \bar{e} (\gamma_\alpha c_{ij} - \gamma_\alpha \gamma_5 b_{ij}) e \equiv -\frac{G_F}{\sqrt{2}} (\mathcal{N}_b^\alpha \bar{e} \gamma_\alpha \gamma_5 e - \mathcal{N}_c^\alpha \bar{e} \gamma_\alpha e), \quad (1)$$

$$\mathcal{N}_b^\alpha = \sum_{ij} b_{ij} \bar{\nu}_i \gamma^\alpha (1 - \gamma_5) \nu_j, \quad \mathcal{N}_c^\alpha = \sum_{ij} c_{ij} \bar{\nu}_i \gamma^\alpha (1 - \gamma_5) \nu_j, \quad (2)$$

$$b_{ij} = U_{ei}^* U_{ej} - \frac{1}{2} \delta_{ij}, \quad c_{ij} = U_{ei}^* U_{ej} - \frac{1}{2} (1 - 4 \sin^2 \theta_w) \delta_{ij} = b_{ij} + 2 \sin^2 \theta_w \delta_{ij}, \quad (3)$$

where ν_i denotes a neutrino of definite mass m_i and θ_w is the weak mixing angle. Electron axial vector current couples to neutrino-pair emission current \mathcal{N}_b^α , while electron vector current couples to pair emission current \mathcal{N}_c^α . Parameters b_{ij}, c_{ij} are known except CP phases that appear in U_{ei} , one phase in the Dirac neutrino case and three phases in the Majorana case. Our strategy of neutrino mass spectroscopy is to assume unknown value m_1 of smallest neutrino mass and CP phases for fixing all other variables, and calculate observable quantities for experimental comparison. This way one does not have to commit to any

particular model beyond the standard theory, except finite neutrino masses and CP violation phases. If CP conservation is assumed, all b_{ij}, c_{ij} 's are real and already known, leaving m_1 as a single unknown parameter. Decomposition of flavor states ν_e into neutrino mass eigenstates ν_i is achieved in our proposed experiments by precision of laser frequencies, usually less than μeV , and not by measurable accuracy of photon energy in detectors that may be larger than 1 meV.

The dominant interference term of parity violation arises from product of spatial part of axial vector current of electron, $\bar{e}\vec{\gamma}\gamma_5 e$ which is the spin operator \vec{S} in the non-relativistic limit of atomic electrons, and spatial part of vector current, the velocity operator $\bar{e}\vec{\gamma}e \sim \langle\vec{v}\rangle = \langle\vec{p}\rangle/m_e$ (nearly equivalent to position operator \vec{r} times energy difference between two involved atomic states, often used in atomic physics). Matrix elements of spin $\langle\vec{S}\rangle$ are usually of order unity, while those of velocity operator $\langle\vec{v}\rangle$ are less than 10^{-3} , hence interference terms are at least smaller by 10^{-3} than rate $\propto \langle\vec{S}\rangle^2$ of a parity even quantity. We shall quantify this ratio for lanthanoid ion we use as a target. Magnetization caused by (ij) neutrino-pair emission is proportional to neutrino mixing parameters, $\Re(b_{ij}c_{ij})$ (assuming CP conservation for simplicity), while parity conserving quantity of RENP event rate is proportional to $\Re(b_{ij}^2)$.

A great advantage of 4f electrons in lanthanoid ions is that they are not sensitive to environmental effects of host crystals due to filled 5s and 5p electrons in outer shells working as a shield. This circumstance gives both a narrow transition width and a large spin relaxation time, the latter being very important to magnetization measurement. Lanthanoid ions of low concentration doped in host crystals exhibit paramagnetic property at room temperature. For an experimental purpose as explained below, we shall use Kramers degenerate ions in which two states of different time reversal quantum numbers \pm are energetically degenerate.

We develop in the present work an improved calculation method of macro-coherent rates and magnetization by incorporating finite size effect of crystal target in integration over neutrino momenta. In the previous works we took the infinite volume limit giving rise to the momentum conservation, or more properly the phase matching condition. But it is difficult to justify this infinite size limit for experimentally used size of targets, of order ≈ 1 cm. This improved method gives quantitatively different results of rate and magnetization, although the phase matching condition may be still useful as a technical guide. Angular distribution of magnetization, the most important physical quantity to neutrino mass spectroscopy, is greatly influenced by change of this calculation method.

The measurement method we propose here is different from those in previous proposals: detection of accumulated magnetization remaining in target medium [6] rather than measuring direct individual events that rarely occur. If the accumulated magnetization is above the sensitivity level of detectors, for instance, a high quality SQUID, then the method is found to be sensitive to absolute neutrino mass determination and to Majorana/Dirac distinction. Proposed experiments can be conducted irrespective of the nature of neutrino masses, Majorana or Dirac, and experiments themselves can determine whether neutrinos are of either type by measuring the shape and the magnitude of angular distribution of generated magnetization. The principle of this distinction is due to existence of interference term intrinsic to identical fermions (particle = anti-particle) in the Majorana neutrino case [9]. In the Dirac neutrino case anti-neutrinos are distinguishable, hence there is no interference.

The present paper is organized as follows. In the next section we first present amplitude of individual atomic process, and in the second next section we spell out improved calculation method of phase factors over entire target atoms incorporating finite size effect of target. In Section 4 we explain trivalent Er ion used as a target candidate and present results of magnetization calculation. Effect of crystal field is quantified and used in calculation of atomic matrix elements. A host crystal was chosen from the point of rich available optical data necessary for detailed computations. In Summary and Outlook of Section 5 we mention points to be studied for realistic experimental design. In Appendix we explain four-level optical Bloch equation and its solutions necessary to estimate populations in energy levels and coherence parameters.

We use the natural unit of $\hbar = c = 1$ throughout the present work unless otherwise stated.

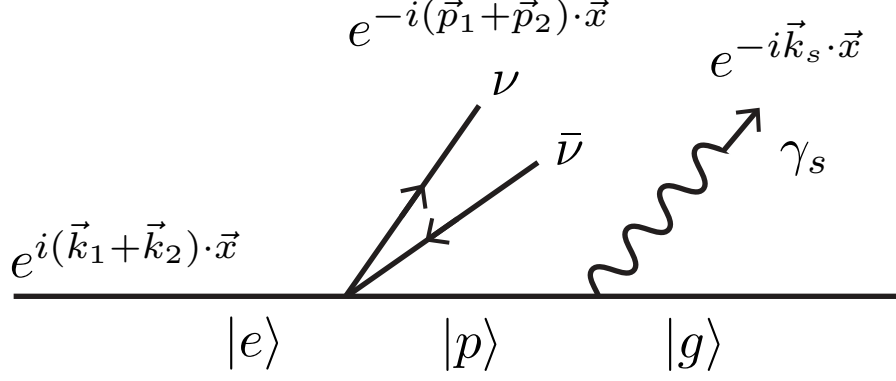


Figure 1: Feynman diagram based on old-fashioned non-relativistic perturbation theory of RENP $|e\rangle \rightarrow |g\rangle + \gamma_s + \nu\bar{\nu}$. Relevant phase factors including imprint to state $|e\rangle$ given by the wave vector, $\vec{k}_1 + \vec{k}_2$, at two-laser excitation are attached to ion and particle states.

2 Probability amplitude of RENP process and parity violating magnetization

A particular class of RENP process we consider in the present work consist of individual events occurring each at a space point \vec{x} . Its diagram is shown in Fig(1). Individual atomic (or ionic) transition probability amplitude is given by

$$\mathcal{A}_{ij} e^{-iK_0 t + i\vec{K} \cdot \vec{x}}, \quad K_0 = \omega_1 + \omega_2 - \omega_s - E_1 - E_2, \quad \vec{K} = \vec{k}_1 + \vec{k}_2 - \vec{k}_s - \vec{p}_1 - \vec{p}_2, \quad (4)$$

$$\mathcal{A}_{ij} = -\frac{G_F (b_{ij} \vec{S}_{ep} + c_{ij} \vec{v}_{ep}) \cdot \vec{N}_{ij} (\vec{d}_{pg} \cdot \vec{E}_t + \vec{\mu}_{pg} \cdot \vec{B}_t)}{\sqrt{2} (\epsilon_{pg} - \omega_s - i\gamma_{ep}/2)}, \quad \vec{N}_{ij} = \bar{\nu}_i \vec{\gamma} (1 - \gamma_5) \nu_j. \quad (5)$$

Neutrino field operators $\nu_i, \bar{\nu}_j$ in Introduction should be replaced here by their plane wave functions, but we shall keep the same notation for simplicity. We prepare excited state $|e\rangle$ by two-photon laser excitation of their photon 4-momenta $(\omega_i, \vec{k}_i), i = 1, 2$ from the ground state $|g\rangle$. Emitted signal photon γ_s is stimulated by trigger laser of photon 4-momentum $(\omega_t, \vec{k}_t) = (\omega_s, \vec{k}_s)$. $(E_i = \sqrt{\vec{p}_i^2 + m_i^2}, \vec{p}_i), i = 1, 2$, are 4-momenta of emitted neutrino pairs with their masses given by m_i, m_j . The second order perturbation theory originally gives an energy denominator, $1/(-\epsilon_{ep} + E_1 + E_2)$, which is transformed as above by using the exact rule of energy conservation $\epsilon_{eg} (= \omega_1 + \omega_2) = \omega_s + E_1 + E_2$, in order to eliminate neutrino energy dependence and make explicit dependence on the fixed signal photon energy ω_s . Two transition dipoles, magnetic ($\vec{\mu}_{pg}$) and electric (\vec{d}_{pg}), are included in trigger field coupling $\propto \vec{E}_t, \vec{B}_t$ where laser intensity I_t is given by the power Watt divided by an area, being related to field strength by $|\vec{E}_t| = |\vec{B}_t| = \sqrt{I_t}$.

In Fig(2) we show momentum relation for target ion we shall consider in the present work. Three momenta, $\vec{k}_1, \vec{k}_2, \vec{k}_s = \vec{k}_t$, those for excitation and trigger, and we assume that they are in a plane, while individual neutrino momenta, $\vec{p}_i, i = 1, 2$, may be out of this plane,

An implicit assumption for RENP amplitude is to be noted: emitted signal photons do not suffer from scattering or any reaction with surrounding atoms in solid after their emission. Even if there are interactions with surrounding atoms leaving modifications of amplitude formula, the subsequent formula for magnetization is valid with RENP amplitude here, since magnetization is generated immediately after RENP and prior to interactions.

When the trigger laser is tuned to the resonance energy ϵ_{pg} , the amplitude becomes

$$\mathcal{A}_{ij} = -i\sqrt{2}G_F h_r (b_{ij} \vec{S}_{ep} + c_{ij} \vec{v}_{ep}) \cdot \vec{N}_{ij}, \quad h_r = \frac{\vec{d}_{pg} \cdot \vec{E}_t + \vec{\mu}_{pg} \cdot \vec{B}_t}{\gamma_{ep}}. \quad (6)$$

Relation of momentum vectors

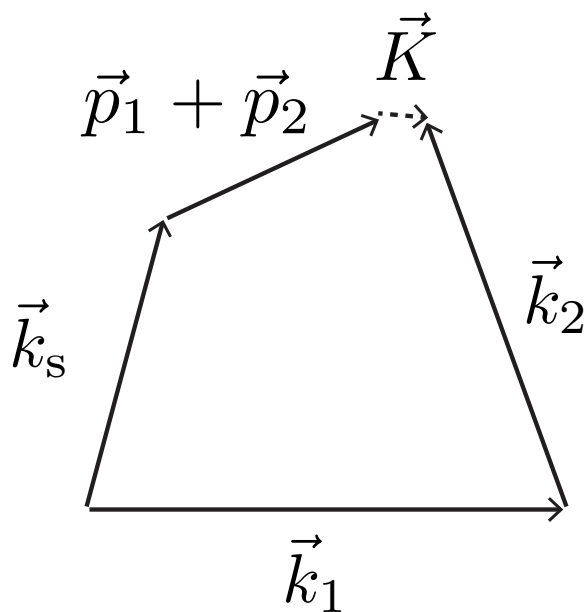


Figure 2: Relation of momentum vectors and definition of \vec{K} with fixed magnitudes, $k_1 = 1.286$, $k_2 = 1.109$, $k_s = 0.805$ in eV unit.

A remarkable feature of this formula is that the RENP amplitude \mathcal{A}_{ij} is equal to neutrino-pair decay amplitude of $|e\rangle \rightarrow |p\rangle + \nu_i \bar{\nu}_j$, simply multiplied by $2h_r$ in which effect of stimulated photon emission is coded.

Let us consider in more detail the factor h_r multiplying the neutrino-pair emission amplitude, which may be related to various observable quantities. We consider unpolarized target and linear polarization of trigger laser consisting of an equal mixture of two circular polarizations. In this case

$$h_r = \sqrt{\frac{\pi}{\epsilon_{pg}^3}} (\sqrt{\gamma_{pg}^{\text{MD}}} + \sqrt{\gamma_{pg}^{\text{ED}}}) \frac{\sqrt{I_t}}{\gamma_{ep}}. \quad (7)$$

In the case of trivalent Er ion scheme later proposed, this combination of parameters is numerically estimated as

$$h_r \sim 2.5 \times 10^3 \sqrt{\frac{I_t}{10 \text{mWcm}^{-2}}}, \quad (8)$$

if one takes radiative decay rate, 57.3 sec^{-1} , for γ_{ep} . If an inhomogeneously broadened width of order $10 \sim 100 \text{ MHz} \times 2\pi$ is taken for γ_{ep} , this number decreases to $2.3 \times (10^{-3} \sim 10^{-4}) \sqrt{I_t/10 \text{mWcm}^{-2}}$. We propose to use lowest Stark levels in each lanthanoid J-manifold, since uncontrollable phonon relaxation is minimal for transitions between these levels. We may leave this uncertainty by inserting $(57.3 \text{ sec}^{-1}/\gamma_{ep})^2$ in subsequent formulas of rate and magnetization.

Neutrino variables, their helicities and momenta, are extremely difficult to measure, especially at these low energies, hence one integrates over these unobservables in atomic experiments. Neutrino helicity sum gives both for electron spin-current and for velocity current, [1]

$$\sum_{h_1, h_2} |\vec{\mathcal{N}}_{ij} \cdot \vec{j}_e|^2 = \frac{1}{2} \left(1 - \frac{\vec{p}_1 \cdot \vec{p}_2}{E_1 E_2} - \delta_M \frac{m_1 m_2}{4E_1 E_2} \right) \vec{j}_e \cdot \vec{j}_e + \frac{\vec{p}_1 \cdot \vec{j}_e \vec{p}_2 \cdot \vec{j}_e}{E_1 E_2} + \dots, \quad (9)$$

where dots \dots give irrelevant T-odd terms. Electron matrix elements of (ij) neutrino pair emission are given by $\vec{j}_e = \bar{e}(\vec{\gamma} c_{ij} - \vec{\gamma} \gamma_5 b_{ij})e$ with e, \bar{e} being replaced by relevant atomic wave function and conjugate of bound electrons states, $|p\rangle, |e\rangle$. $\delta_M = 0$ for Dirac neutrino and $\delta_M = 1$ for Majorana neutrino. Directional average over electron current \vec{j}_e may be taken for unpolarized targets, which gives the last term of the form, $\vec{p}_1 \cdot \vec{p}_2 / (3E_1 E_2)$. Neutrino variable dependence in $|\mathcal{A}_{ij}|^2$ is then a function of $\vec{p}_1 \cdot \vec{p}_2$ depending on the opening angle θ_{12} and magnitudes $p_i, i = 1, 2$.

Presence of crystal field is important to make it possible to measure parity violating effect of fundamental interaction. Both of RENP initial and final states, $|e\rangle$ and $|f\rangle$, are eigenstates of QED interaction, including static Coulomb interaction of target ion with host crystal ions, which is a crystal field effect. Relevant parity violating quantity of our interest $\langle f | \hat{k} \cdot \vec{S}_e | f \rangle$ is transformed by parity operation P to $-\langle f | P^{-1} \hat{k} \cdot \vec{S}_e P | f \rangle$. Hence crystal field effect must produce parity mixture in the state $|f\rangle$; $|f\rangle = |f\rangle_+ + |f\rangle_-$ such that $\langle f | \hat{k} \cdot \vec{S}_e | f \rangle = \langle f | \hat{k} \cdot \vec{S}_e | f \rangle_- + \langle f | \hat{k} \cdot \vec{S}_e | f \rangle_+$ in order to have non-vanishing value of $\langle f | \hat{k} \cdot \vec{S}_e | f \rangle = -\langle f | P^{-1} \hat{k} \cdot \vec{S}_e P | f \rangle$.

The crystal field V_c acting on a lanthanoid $4f^n$ ion contains mixture of parity different states due to interaction with surrounding host crystal ions: by decomposing state vector into $|4f\rangle = |4f\rangle_0 + \delta|4f\rangle$ with $|4f\rangle_0$ defined as state without crystal field, one has

$$\delta|4f\rangle \simeq \left(\frac{\partial V_c}{\partial \vec{r}} \right)_{\vec{r}=0} \cdot \langle 5d | \vec{r} | 4f \rangle |5d\rangle,$$

as pointed out by [7]. This peculiar situation, which does not occur for isolated atoms in the free space, arises naturally when lanthanoid ions are placed in crystals. It is known that low-lying lanthanoid ions of $4f^n$ system are ordinarily activated by magnetic dipole transitions, but can often simultaneously have forced electric dipole transitions of different parity, being caused by crystal field [7]: its calculation method was formulated in [8].

3 Improved calculation method of macro-coherent RENP rate

We re-examine and improve the calculation method of macro-coherent RENP rate and persistent magnetization, directly summing over plane-wave factors of relevant absorbed and emitted particles. Suppose that one wants to determine energy and momentum to an accuracy level, $(100 \sim 1)\mu\text{eV}$, whose inverse corresponds to $6.6 \times (10^{-12} \sim 10^{-10})$ sec in time and $2 \sim 200$ cm in length. Time scale given here is much smaller than the usual measurement time of atomic experiments, which implies that the Fermi golden rule of the infinite time limit should be valid and the energy conservation holds. The length scale, on the other hand, is larger than a typical spatial region of actual experiments, < 1 cm. Hence one cannot take the infinite size limit giving the momentum conservation of macro-coherent rates. What is achieved in the present improved method is incorporation of finite size effect by which it becomes possible to deal with intricate double resonance region of dynamical variables.

We investigate total event rate emerging from $N = nV$ atoms or ions in a target volume of cylinder, $V = \pi R^2 L$, irradiated by excitation and trigger lasers. Event of an individual target atom/ion at a position \vec{x} contributes to the total amplitude a piece proportional to product of plane waves of absorbed and emitted particles, $e^{i\vec{K}\cdot\vec{x}}\mathcal{A}_{ij}$ (\vec{K} = sum of an imprint wave vector + relevant momenta of emitted particles), with the atomic amplitude \mathcal{A}_{ij} independent of \vec{x} position. We need to calculate an elementary integral of squared amplitude over neutrino momenta,

$$\int \frac{d^3 p_1 d^3 p_2}{(2\pi)^6} 2\pi\delta(K_0) |\mathcal{A}|^2 I, \quad I = (|\chi|n)^2 \left| \int_V d^3 x \exp[i\vec{K}\cdot\vec{x}] \right|^2, \quad (10)$$

for the triggered process $|e\rangle \rightarrow |g\rangle + \gamma_s + \nu\bar{\nu}$. Here n is the target ion number density assumed constant. The averaged coherence $|\chi|$ may be estimated by solving an optical Bloch equation, as discussed later.

In the previous simplified treatment [1], [4], [6], we took the infinite volume limit which gives the space integral of the form,

$$\left| \int_V d^3 x \exp[i\vec{K}\cdot\vec{x}] \right|^2 = V (2\pi)^3 \delta(\vec{K}).$$

How this result is changed for a large, but finite volume is a subject of this section.

For a target region of cylinder, radius R and length L , its volume $V = \pi R^2 L$ (having in mind $R \ll L = O(1)$ cm), the spatial integration of phase factors in eq.(10) gives

$$\int_V d^3 x \exp[i\vec{K}\cdot\vec{x}] = A_1 A_2, \quad A_1 = \frac{2 \sin \frac{K_z L}{2}}{K_z}, \quad A_2 = 2\pi \frac{R}{K_\perp} J_1(K_\perp R), \quad (11)$$

$$|A_1 A_2|^2 = V^2 U\left(\frac{K_z L}{2}\right) W(K_\perp R), \quad U(x) = \left(\frac{\sin x}{x}\right)^2, \quad W(y) = \left(2 \frac{J_1(y)}{y}\right)^2, \quad (12)$$

where $K_\perp (K_z)$ is the magnitude of transverse(longitudinal) component to cylinder axis of excitation (parallel to the first excitation laser photon \vec{k}_1). $J_1(z)$ ($\sim z/2$ as $z \rightarrow 0$) is the Bessel function of the first order.

Both functions $U(x), W(y)$ decrease as arguments $|x|$ or $|y|$ increases, showing damped oscillatory behaviors. It is difficult to accurately incorporate these damped oscillations in numerical integration over neutrino momenta, $\int d^3 p_1 d^3 p_2$. We thus replace these by a smoothed out function, either Lorentzian function or gaussian function. It was found that Lorentzian functions are easier to handle from the point of numerical computations.

The necessary neutrino-pair phase space integral for rate of RENP process, $|e\rangle \rightarrow |g\rangle + \gamma_s + \nu\bar{\nu}$, depends on how spin matrix element \vec{S}_{ep} (and smaller \vec{v}_{ep} , too) in the amplitude, eq.(6), is oriented. In order to simplify unnecessary complications, we shall assume for the sake of discussion here the case in which contributions proportional to $\vec{S}_{ep} \cdot \vec{p}_1 \vec{S}_{ep} \cdot \vec{p}_2$ averages out to give vanishing contribution. More realistic spin and velocity

orientations shall be discussed in Section 4. Assuming the azimuthal symmetry, RENP rate is given by

$$\frac{h_r^2 G_F^2}{(2\pi)^3} (nV)^2 |\chi|^2 |\vec{S}_{ep}|^2 \sum_{ij} \mathcal{F}_{ij}^{(0)}, \quad \mathcal{F}_{ij} = \int dE_1 \int dE_2 \delta(E_1 + E_2 - \epsilon_{ep}) \sqrt{E_1^2 - m_i^2} \sqrt{E_2^2 - m_j^2} \cdot \int_{-\pi}^{\pi} d\theta_1 \int_{-\pi}^{\pi} d\theta_2 |\sin \theta_1 \sin \theta_2| U_0\left(\frac{K_z L}{2}\right) W_0(K_{\perp} R) \mathcal{R}_{ij}, \quad (13)$$

$$U_0(x) = \frac{1}{1 + (x/x_l)^2}, \quad x_l = 1, \quad W_0(y) = \frac{1}{1 + (y/y_t)^2}, \quad y_t = \frac{32}{3\pi^2} \simeq 1.081, \quad (14)$$

$$x = \frac{L}{2} (p_1 \cos \theta_1 + p_2 \cos \theta_2 - w_l), \quad w_l = (\omega_1 + \omega_2 \cos \theta_e - \omega_s \cos \theta_s) n_r, \quad (15)$$

$$y = \frac{R}{y_t} (p_1 \sin \theta_1 + p_2 \sin \theta_2 - w_t), \quad w_t = (\omega_2 \sin \theta_e - \omega_s \sin \theta_s) n_r, \quad (16)$$

with n_r the index of refraction of host crystal (~ 1.45 in host crystal of Section 4). \mathcal{R}_{ij} is a function of (E_i, \vec{p}_i) , $i = 1, 2$ up to bi-linear orders, and shall be explicitly given below in eq.(48) for each neutrino (ij) pair. Lorentzian parameters x_l, y_t were determined by requiring that Lorentzian functions coincide with exact plane-wave integrals of $U(x) = (\sin x/x)^2$, $W(y) = (2J_1(y)/y)^2$ in values at $x = 0, y = 0$ and integrated values. All angles are measured from z-axis of the first excitation laser.

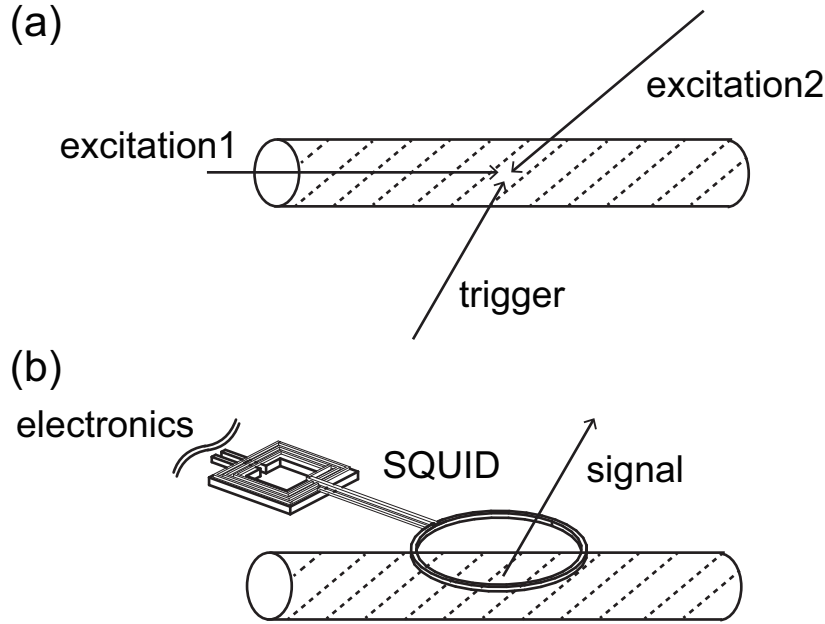


Figure 3: (a) Excitation scheme. (b) Detection scheme along with signal photon.

For large values of L, R , two Lorentzian functions, $U_0(x), W_0(y)$, have sharp peaks in neutrino variables at $x = 0, y = 0$, which restricts the region of largest contribution in the neutrino phase space integral given by three independent variables, p_1, θ_1, θ_2 . The largest region is given by $\vec{K} = 0$ where $\vec{K} = \vec{k}_1 + \vec{k}_2 - \vec{p}_1 - \vec{p}_2 - \vec{k}_s$, and momentum vector relation is depicted in Fig(2). Thresholds of neutrino-pair production are given by taking vanishing neutrino momenta $\vec{p}_i = 0$. The threshold condition gives $w_t = 0, w_l = 0$, or

$$\omega_2 \sin \theta_e - \omega_s \sin \theta_s = 0, \quad \omega_2 \cos \theta_e - \omega_s \cos \theta_s = -\omega_1. \quad (17)$$

This determines both θ_s, θ_e : in resonant trivalent Er scheme, energies ω_i, ω_s are all fixed, and two angles are determined as $\cos \theta_e = -0.7838, \cos \theta_s = 0.5182$ (142 and 59 degrees). Thus, introduction of non-aligned

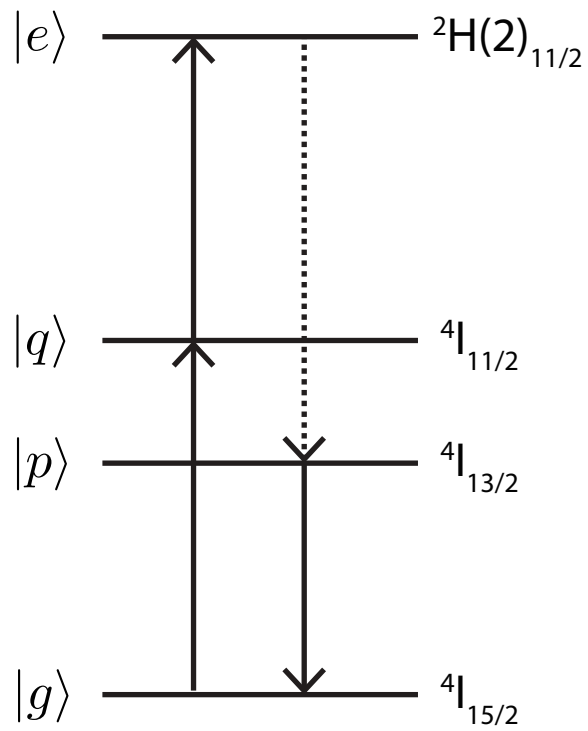


Figure 4: Excitation and trigger laser scheme for trivalent Er, both depicted in arrowed solid lines, and neutrino-pair emission depicted in arrowed dotted line.

second excitation laser of $\theta_e \neq 0, \pi$ is required to experimentally approach neutrino-pair thresholds which are most sensitive to Majorana/Dirac distinction.

Numerical pre-factor to be multiplied to $|\chi|^2 |\vec{S}_{ep}|^2 \sum_{ij} \mathcal{F}_{ij}$ is

$$C = \frac{h_r^2 G_F^2}{(2\pi)^3} (nV)^2 = 6.3 \times 10^{11} \text{ sec}^{-1} \text{ eV}^{-5} \frac{57.3 \text{ sec}^{-1}}{\gamma_{ep}} \frac{I_t}{10 \text{ mW cm}^{-2}} \left(\frac{R}{0.5 \text{ cm}}\right)^4 \left(\frac{L}{\text{cm}}\right)^2 \left(\frac{n}{1.4 \times 10^{19} \text{ cm}^{-3}}\right)^2, \quad (18)$$

with $V = 0.785 \text{ cm}^3 (R/0.5 \text{ cm})^2 L/\text{cm}$. The number in front is changed as $6.3 \times 10^{11} \rightarrow 6.0 \times (10^5 \sim 10^4)$, if one takes $10 \sim 100 \text{ MHz} \times 2\pi$ for γ_{ep} .

4 Trivalent Er ion scheme

In the present work we shall restrict to cases of neutrino pair emission, in which two-photon excitation from the ground state to excited state $|e\rangle$ is followed by triggered RENP: $|g\rangle + \gamma_1 + \gamma_2 \rightarrow |e\rangle$; $|e\rangle \rightarrow |g\rangle + \gamma_s + \nu\bar{\nu}$. Experimental layout is shown in Fig(3). Excitation laser and trigger laser frequencies are matched to level spacings of trivalent Er ion as shown in Fig(4).

Typical candidate targets we may consider are trivalent Er and Ho ions which have odd (11) and even (10) number of 4f valence electrons, respectively. Trivalent $4f^{11}$ Er ion has Kramers degeneracy, degeneracy due to time reversal invariance, while Ho ion does not have this degeneracy automatically. Symmetry of host crystal may however induce accidental Kramers degeneracy in non-singlets. This occurs in the ground state of Ho^{3+} in a special host crystal of higher symmetry.

Lanthanoid ions in the free space, or vacuum, are classified using the LS coupling scheme, giving multiplets $2S+1L_J$ in which J is the total angular momentum combining the total spin S and the total orbital L angular momentum. In the ground state of trivalent Er ion, $S = 3/2$ and $L = 6$, $J = 15/2$, and is denoted by a term notation $^4I_{15/2}$. These multiplets, called J-manifolds, are split into Stark states under crystal field of host crystals, as illustrated in Fig(5). Typical J-manifold splitting is of order $0.5 \sim 1 \text{ eV}$, while Stark splitting is of order several tens of meV [11]. The number of separated Stark states in J-manifold is $J + 1/2$ for half-odd J , each forming Kramers doublets, whose degeneracy may be lifted, with amount of order $60 \mu\text{eV B}/\text{Tesla}$, by application of magnetic field. Relaxation due to phonons in solids, which might become serious obstacles against RENP, is the smallest at the lowest Stark state in each J-manifold, hence we shall use the lowest Stark states of J-manifold in optical transitions.

The choice of host crystals is important for success of RENP project. We choose LiYF_4 (usually called YLF) crystal as host. This crystal has a point group symmetry S_4 at the site of F, and target ion Er^{3+} replaces a fraction of F sites. Energy levels of Stark states in doped crystal $\text{Er}^{3+}:\text{YLF}$ are well known, but we further need magnetic and electric dipole transition rates denoted by MD and ED. For these we have to use available theoretical calculation of different, but similar host crystal $\text{Er}^{3+}:\text{Cs}_2\text{NaYF}_6$. According to [12], calculated radiative decay rates of 10% doped Er^{3+} in host Cs_2NaYF_6 and other data are

initial	final	energy/eV	radiative decay rate/sec ⁻¹	$v/S(10^{-6})$
$^4I_{13/2} \rightarrow$	$^4I_{15/2}$	0.805	$24.82^{\text{MD}} + 2.46^{\text{ED}}$	0.25
$^4I_{11/2} \rightarrow$	$^4I_{15/2}$	1.286	4.13^{ED}	
	$^4I_{13/2}$	0.481	$4.26^{\text{MD}} + 0.42^{\text{ED}}$	0.15
$^2H_{11/2} \rightarrow$	$^4I_{15/2}$	2.3946eV	518.02^{ED}	
	$^4I_{13/2}$	1.5894eV	$49.43^{\text{MD}} + 7.91^{\text{ED}}$	1.2
	$^4I_{11/2}$	1.1091eV	$5.58^{\text{MD}} + 4.73^{\text{ED}}$	1.0
	$^4I_{9/2}$	0.8318eV	$0.49^{\text{MD}} + 5.52^{\text{ED}}$	2.7

Coexistence of magnetic and electric dipole transitions, a necessary ingredient for magnetization measurement in RENP, is a manifestation of forced electric dipole moment in lanthanoid crystals [7], [8]. We

have also shown in the last column the ratio of vector and spin current matrix elements calculated from radiative decay rates.

Our RENP scheme of trivalent Er ion uses the following J-manifolds as in Fig(4):

$$\text{de - excitation; } |e\rangle = {}^2\text{H}_{11/2}(2.3946 \text{ eV}) \rightarrow |p\rangle = {}^4\text{I}_{13/2}(0.805 \text{ eV}) \rightarrow |g\rangle = {}^4\text{I}_{15/2}(0 \text{ eV}), \quad (19)$$

$$\text{excitation; } {}^4\text{I}_{15/2}(0 \text{ eV}) \rightarrow |q\rangle = {}^4\text{I}_{11/2}(1.286 \text{ eV}) \rightarrow {}^2\text{H}_{11/2}(2.3946 \text{ eV}). \quad (20)$$

Hence excitation and trigger(=signal) laser energies in eV unit are

$$\omega_1 = 1.286, \quad \omega_2 = 1.1086, \quad \omega_s = \omega_t = 0.805. \quad (21)$$

The expected position of neutrino pair thresholds calculated from eq.(17) appears at signal (=trigger) direction given by

$$\cos \theta_s = \frac{\omega_1^2 - \omega_2^2 + \omega_s^2}{2\omega_1\omega_s} \sim 0.518, \quad (22)$$

corresponding to $\pm 1.026(\pm 59)$ radians(degrees). The second excitation laser should be irradiated with aligned angle at

$$\cos \theta_e = -\frac{\omega_1^2 + \omega_2^2 - \omega_s^2}{2\omega_1\omega_2} \sim -0.784, \quad (23)$$

corresponding to $\pm 2.47(\pm 140)$ radians(degrees).

Optical and neutrino-pair emission processes in solids are governed by the selection rule of time reversal (T) quantum number: its change must be T-odd, since two major single-photon operators, electric dipole (E1) \vec{p}/m_e and magnetic dipole (M1) $\vec{\mu}$, and neutrino-pair emission operators, \vec{S} and \vec{v} , are all T-odd. (Use of the length gauge $e\vec{r}$ for E1 obscures this nature of T-oddness.) On the other hand, two-photon excitation is governed by T-even operator, hence $|e\rangle$ and $|g\rangle$ are both T-even or both T-odd [13]. The intermediate state $|p\rangle$ that participates in neutrino-pair emission has different T quantum number from these.

States constructed in the LS coupling scheme

$$|\psi\rangle = a_J|J, M_J\rangle + b_{J'}|J', M'_{J'}\rangle + \dots, \quad (24)$$

are transformed under time reversal to

$$T|\psi\rangle = (-1)^{J+M_J} a_J^*|J, -M_J\rangle + (-1)^{J'+M'_{J'}} b_{J'}^*|J', -M'_{J'}\rangle + \dots. \quad (25)$$

In the leading order of our scheme, $(-1)^{J+M_J} = 1$. The second terms $\propto b_{J'}$ are sub-leading compared to $\propto a_J$ terms. States of $T = \pm$ are constructed as

$$\frac{1}{\sqrt{2}}(1 \pm T)|\psi\rangle \equiv |\psi^\pm\rangle. \quad (26)$$

Matrix elements of T-odd operator V are then given by

$$\langle \psi_2^- | V | \psi_1^+ \rangle = a_{J_2}^* a_{J_1} \langle J_2, M_{J_2} | V | J_1, M_{J_1} \rangle + (-1)^{J_1+M_{J_1}} a_{J_2}^* a_{J_1}^* \langle J_2, M_{J_2} | V | J_1, -M_{J_1} \rangle \quad (27)$$

to leading orders. The first term dominates over the second term due to smaller ΔM_J .

Crystal field acting on trivalent Er ion (sum of Coulomb interaction caused by surrounding host ions) splits J-manifold states into $J + 1/2$ degenerate Kramers doublets, consisting of T-even and -odd linear combinations of $\sum_{M_J} c_{M_J > 0} (|J, M_J\rangle \pm (-1)^{J+M_J} |J, -M_J\rangle)$ with quantization axis taken parallel to c-axis of tetragonal host crystal. Magnetic quantum numbers of lowest Stark levels for relevant RENP J-manifolds

are mixtures of different M_J values, and their weights are calculated using tabulated crystal field parameters [14]. Our calculation shows that dominant components have probabilities,

$$|e\rangle {}^2\text{H}_{11/2}(\Gamma_{78} \text{ of } S_4); M_J = \pm\frac{1}{2} : 0.1547, \quad M_J = \pm\frac{7}{2} : 0.2401, \quad (28)$$

$$|p\rangle {}^4\text{I}_{13/2}(\Gamma_{56}); M_J = \pm\frac{3}{2} : 0.2559; , \quad M_J = \pm\frac{5}{2} : 0.1227, \quad (29)$$

$$|g\rangle {}^4\text{I}_{15/2}(\Gamma_{78}); M_J = \pm\frac{5}{2} : 0.2002, \quad M_J = \pm\frac{3}{2} : 0.1374. \quad (30)$$

Γ_{78}, Γ_{56} denote irreducible representations of relevant S_4 point group of host crystal. Neutrino pair emission at $|e\rangle \rightarrow |p\rangle$ followed by stimulated photon emission at $|p\rangle \rightarrow |g\rangle$ can occur, going through states of magnetic quantum number changes, $M_J = \pm 1/2 \rightarrow \pm 3/2 \rightarrow \pm 5/2$ by minimum steps of $\Delta M_J = \pm 1$. This path gives the largest contribution.

We need to calculate matrix elements of $\vec{S}_{ep}, \vec{v}_{ep}, \vec{\mu}_{pg} = \mu_B(\vec{J} + \vec{S})_{pg}, \vec{d}_{pg} = ie\vec{v}_{pg}/\epsilon_{pg}$, including necessary crystal field effect. Calculation of spin matrix elements uses mixing amplitude times 3j-symbol. For neutrino pair emission at $|e\rangle \rightarrow |p\rangle$,

$$\langle p; \frac{13}{2}, \Gamma_{56} | S_+ | e; \frac{11}{2}, \Gamma_{78} \rangle = 0.199 (= \sqrt{0.1547 \times 0.2559} (-1)^{13/2-3/2} \begin{pmatrix} \frac{13}{2} & 1 & \frac{11}{2} \\ -\frac{3}{2} & 1 & \frac{1}{2} \end{pmatrix}) \langle p; \frac{13}{2} || S || e; \frac{11}{2} \rangle.$$

For this choice of $M_J = 1/2, M'_J = 3/2$, other spin components, matrix elements of S_0, S_- vanish. This means that vector matrix elements are parallel to crystal c-axis.

For estimate of $\vec{v}_{ep} = \pm i \vec{d}_{ep} \epsilon_{ep} / e$ we need to consider the crystal field effect of host crystals, since parity forbids dipole elements between the same parity J-states. The leading effect of host crystal surrounding target ion at l is to introduce Coulomb potential of the form,

$$\left(\sum_l \vec{\nabla} V_C(\vec{r}_l - \vec{r}) \right)_{\vec{r}=0} \cdot \vec{r}, \quad \left(\sum_l \vec{\nabla} V_C(\vec{r}_l - \vec{r}) \right)_{\vec{r}=0} = O\left(\frac{10\text{eV}}{a}\right), \quad (31)$$

with a the lattice constant. Thus, a direct product of two vector operators for instance,

$$\frac{\left(\sum_l \vec{\nabla} V_C(\vec{r}_l - \vec{r}) \right)_{\vec{r}=0}}{\Delta E} \langle p; \frac{13}{2}, M' | (r_0 v_+ + r_+ v_0) | e; \frac{11}{2}, M \rangle, \quad (32)$$

is non-vanishing, where ΔE is a typical energy difference of 5d-4f ionic levels (roughly of order 10 eV). In Judd-Ofelt theory higher order terms $O(r^{2n+1})$ in crystal field expansion and higher levels than 5d are effectively taken into account.

RENp amplitude is finally given in terms of reduced matrix elements which are related to observables. The following general formula for calculation of reduced matrix element of a vector operator is useful:

$$\sum_{m'q} |\langle j+1, m' | A_q | j, m \rangle|^2 = \frac{1}{2j+1} |\langle j+1 || A || j \rangle|^2. \quad (33)$$

For application to the spin operator, we first note a relation in LS coupling scheme,

$$\langle J+1 | \vec{S} | J \rangle = \langle J+1 | \vec{S} + \vec{J} | J \rangle = \langle J+1 | \vec{L} + 2\vec{S} | J \rangle, \quad (34)$$

which gives, when multiplied by the Bohr magneton μ_B , magnetic dipole operator \vec{M} . Hence,

$$|\langle p; \frac{13}{2} || S || e; \frac{11}{2} \rangle|^2 = \frac{12}{\mu_B^2} \sum_{m'q} |\langle p; \frac{13}{2}, m' | M_q | e; \frac{11}{2}, m \rangle|^2 = 12 \frac{3\pi \gamma_{ep}^{MD}}{\mu_B^2 \epsilon_{ep}^3}. \quad (35)$$

Application of this formula to velocity operator requires crystal field effect, giving

$$|\langle p; \frac{13}{2} || V_{\text{crys}} v || e; \frac{11}{2} \rangle|^2 = \frac{12\epsilon_{ep}^2}{e^2} \sum_{m'q} |\langle p; \frac{13}{2}, m' | d_q | e; \frac{11}{2}, m \rangle|^2 = 12 \frac{3\gamma_{ep}^{ED}}{4\alpha\epsilon_{ep}}. \quad (36)$$

Numerically, we find for trivalent Er scheme,

$$\langle p; \frac{13}{2} || S || e; \frac{11}{2} \rangle \approx 3.47, \quad \langle p; \frac{13}{2} || v || e; \frac{11}{2} \rangle \approx 2.79 \times 10^{-6} \quad (37)$$

These give $\vec{S}_{ep}^2 \approx 0.0157$ for lowest Stark states in our scheme.

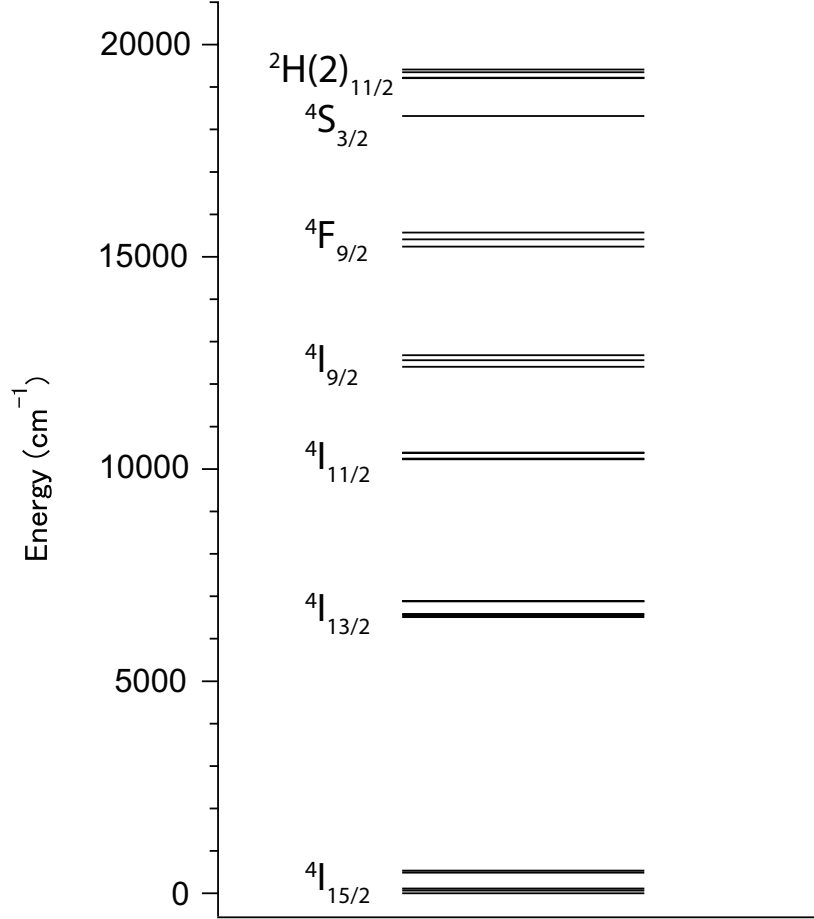


Figure 5: Low-lying trivalent Er levels doped in Cs₂NaYF₆ crystal. Nearly identical, and unresolved with resolution of this figure, level structures appear in YLF host crystal. The energy conversion formula is $1 \times 10^4 \text{cm}^{-1} = 1.238 \text{eV}$.

In order to work out parity violating interference term, we start from squared amplitude when neutrino helicities are specified (not summed over), although neutrino helicities cannot be measured. This calculation gives more insight than providing helicity summed squared amplitude from the outset. Neutrino pair emission of two plane-wave modes specified by their momenta and helicities, $(\vec{p}_1 h_1)$, $(\vec{p}_2 h_2)$, 1 and 2 referring to anti-neutrino (distinguishable from neutrino only for Dirac case) and neutrino variables, respectively, gives

interference term of squared amplitude at $|e\rangle \rightarrow |p\rangle$ [15]

$$(I_{PV})_{12} = 2 \sum_{ij} \Re(v_i \mathcal{N}_{12}^i (\mathcal{N}_{12}^j)^\dagger S_j) = \left\{ C_1 \vec{v} \cdot \vec{S} + C_2 \left(\hat{p}_1 \cdot \vec{v} \hat{p}_2 \cdot \vec{S} + \hat{p}_1 \cdot \vec{S} \hat{p}_2 \cdot \vec{v} \right) \right\} (N_{12} - \delta_M \frac{m_1 m_2}{16 E_1 E_2}) \quad (38)$$

$$C_1 = (1 + h_1 h_2 \frac{\vec{p}_1 \cdot \vec{p}_2}{p_1 p_2}), \quad C_2 = -h_1 h_2, \quad N_{12} = \frac{1}{4} (1 + h_1 \frac{p_1}{E_1}) (1 - h_2 \frac{p_2}{E_2}), \quad (39)$$

$$\vec{p}_1 \cdot \vec{p}_2 = p_1 p_2 \cos \theta_{12}, \quad \hat{p}_i = \frac{\vec{p}_i}{p_i}, \quad (40)$$

where θ_{12} is the opening angle of emitted neutrino-pair, and \hat{p}_i is neutrino propagation vector of unit length.

Two important limiting cases of quantity $(I_{PV})_{12}$ are listed in the following tables; the case of relativistic (R) neutrinos and the case of non-relativistic (NR) neutrinos. The relativistic case gives dominant helicity combination of left-handed neutrino and right-handed anti-neutrino (opposite helicity combination for Majorana neutrino pair), all other combinations giving vanishing contribution. The non-relativistic case gives a different picture of nearly all non-vanishing helicity-combination, as shown in the table.

R-case of $(I_{PV})_{12}$

(h_1, h_2)	\overline{C}_1	\overline{C}_2	comments
(1, -1)	$1 - \cos \theta_{12}$	1	common to Majorana and Dirac
(1, 1)	0	0	common to MD
(-1, 1)	0	0	common to MD
(-1, -1)	0	0	common to MD
Sum	$1 - \cos \theta_{12}$	1	common to MD

The following definition was used; $\overline{C}_i = C_i (N_{12} - \delta_M \frac{m_1 m_2}{16 E_1 E_2})$, $i = 1, 2$.

NR-case of $(I_{PV})_{11}$, assuming an equal mass pair of $m_i = m$, $i = 1, 2$

(h_1, h_2)	\overline{C}_1	\overline{C}_2	comments
(1, -1)	$\frac{1}{4} (1 + \frac{p_1 + p_2}{m} - \frac{\delta_M}{4}) (1 - \cos \theta_{12})$	$\frac{1}{4} (1 + \frac{p_1 + p_2}{m} - \frac{\delta_M}{4})$	$\delta_M = 1(0)$ for Majorana (Dirac)
(1, 1)	$\frac{1}{4} (1 + \frac{p_1 - p_2}{m} - \frac{\delta_M}{4}) (1 + \cos \theta_{12})$	$-\frac{1}{4} (1 + \frac{p_1 - p_2}{m} - \frac{\delta_M}{4})$	
(-1, 1)	$\frac{1}{4} (1 - \frac{p_1 + p_2}{m} - \frac{\delta_M}{4}) (1 - \cos \theta_{12})$	$\frac{1}{4} (1 - \frac{p_1 + p_2}{m} - \frac{\delta_M}{4})$	
(-1, -1)	$\frac{1}{4} (1 - \frac{p_1 - p_2}{m} - \frac{\delta_M}{4}) (1 + \cos \theta_{12})$	$-\frac{1}{4} (1 - \frac{p_1 - p_2}{m} - \frac{\delta_M}{4})$	
Sum	$\frac{3}{4} (1)$	$0(0)$	Majorana (Dirac)

The helicity-summed interference term relevant to actual experiments is given by

$$\sum_{h_1, h_2} C_1 (N_{12} - \delta_M \frac{m_1 m_2}{16 E_1 E_2}) = 1 - \frac{\vec{p}_1 \cdot \vec{p}_2}{E_1 E_2} - \delta_M \frac{m_1 m_2}{4 E_1 E_2}, \quad \sum_{h_1, h_2} C_2 (N_{12} - \delta_M \frac{m_1 m_2}{16 E_1 E_2}) = \frac{p_1 p_2}{E_1 E_2} \quad (41)$$

This result is equivalent to eq.(9) in the preceding section. Neutrino pair phase space integration over momenta of $(I_{PV})_{12}$ further gives PV interference contribution,

$$\tilde{F}_{PV} = \tilde{J}_1 \vec{v} \cdot \vec{S} + (v_i S_j + S_i v_j) \tilde{J}_2^{ij}, \quad (42)$$

$$\tilde{J}_1 = \int dE_1 \int dE_2 \delta(E_1 + E_2 - \epsilon_{ep}) \int_{-\pi}^{\pi} d\theta_1 |\sin \theta_1| \int_{-\pi}^{\pi} d\theta_2 |\sin \theta_2| p_1 p_2 U_0(x) W_0(y) \cdot (E_1 E_2 - \vec{p}_1 \cdot \vec{p}_2 - \delta_M m_1 m_2), \quad (43)$$

$$\tilde{J}_2^{ij} = \int dE_1 \int dE_2 \delta(E_1 + E_2 - \epsilon_{ep}) \int_{-\pi}^{\pi} d\theta_1 |\sin \theta_1| \int_{-\pi}^{\pi} d\theta_2 |\sin \theta_2| p_1 p_2 U_0(x) W_0(y) p_1^i p_2^j. \quad (44)$$

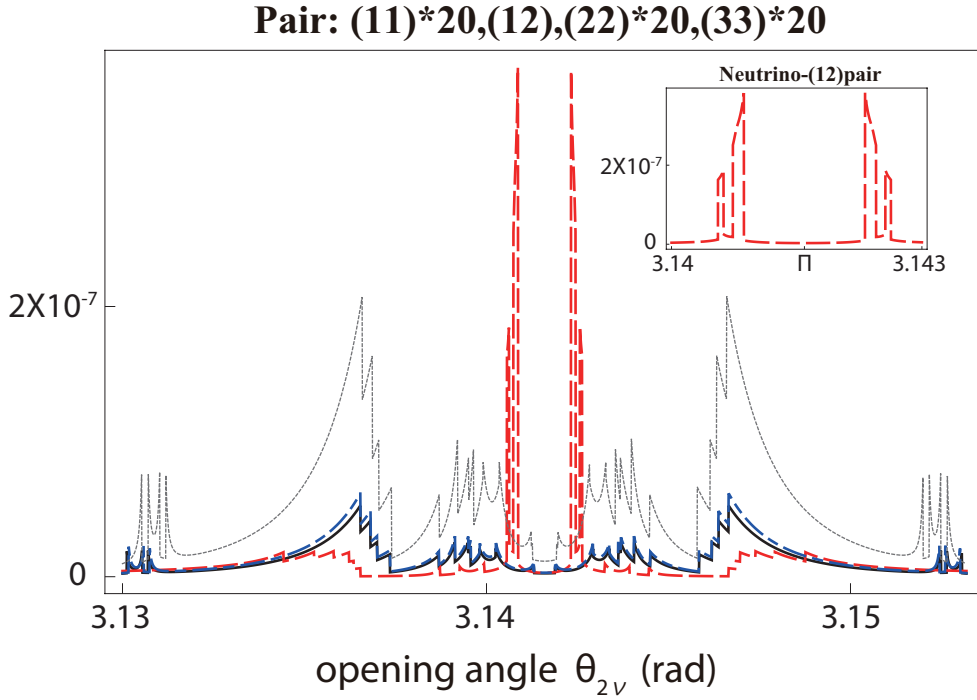


Figure 6: Opening angle distributions from individual neutrino pair contributing to PV term \mathcal{F}_{PV} (in eV^5 unit): (11) pair value times 20 in solid black, (12) in dashed red, (22) times 20 in dash-dotted blue, and (33) times 20 in dotted black. In the inset is shown an enlarged angular structure closer to the back to back pair of $\theta_{2\nu} = \pi$. $\theta_s = 1.026$ and NH Dirac case of smallest neutrino mass 10 meV are assumed.

This gives contribution from a single neutrino-pair, and one should further add all six pair contributions with appropriate weights.

Opening angle ($\theta_{2\nu}$) distributions of neutrino pairs given by \tilde{F}_{PV} , integrated over $\theta_i, i = 1, 2$ with constraint $\theta_1 - \theta_2 = \theta_{2\nu}$, around $\theta_{2\nu} = \pi$ show a rich variety of structures as illustrated in Fig(6) when the signal photon direction is chosen at $\theta_s = 1.026$. A (12) pair gives largest peaks in the form of a (nearly back to back) split doublet with side bands, while other (11), (22), and (33) pairs give widely separated and smaller complicated structures, which is shown in Fig(6) for normal hierarchical (NH) Dirac neutrinos of smallest neutrino mass 10 meV. We have confirmed that angular structure of similar complexity appears for a single massless neutrino pair emission. The angular structure of this complexity results from improved and precise calculation of finite size target effect. It is expected that this structure is reflected in angular distributions of RENP rate and magnetization, which is discussed subsequently.

On the other hand, RENP rate is given by parity conserving quantity taking dominant spin current contribution,

$$\tilde{F}_{PC} \simeq \tilde{J}_1 \vec{S}^2 + 2S_i S_j \tilde{J}_2^{ij}. \quad (45)$$

Details of RENP rate and magnetization depend on how crystals are placed relative to directions of excitation and trigger laser irradiation. Crystal c-axis defines quantization axis and matrix element \vec{S}_{ep} is oriented along this axis due to the selection rule, $\langle J', M+1 | S_i | J, M \rangle = 0$ unless $S_i = S_+$. For simplicity we take direction of the first laser excitation \vec{k}_1 , either parallel or orthogonal to c-axis. There are two important cases of interest: (1) c-axis is parallel to \vec{k}_1 , (2) c-axis is not parallel to \vec{k}_1 , but in the plane spanned by two vectors, \vec{k}_1, \vec{k}_2 , (3) c-axis orthogonal to the plane spanned by these two vectors. We assume that the signal wave-vector \vec{k}_s in \vec{k}_1, \vec{k}_2 plane. In the neutrino phase space integral of \tilde{J}_2^{ij} for case (3) $\vec{p}_i \cdot \vec{S}_{ep}$ and $\vec{p}_i \cdot \vec{v}_{ep}$ give odd functions to integrands, leading to vanishing \tilde{J}_2^{ij} contribution. Hence $\tilde{F}_{PV} = \tilde{J}_1 \vec{v}_{ep} \cdot \vec{S}_{ep}$ and $\tilde{F}_{PC} = \tilde{J}_1 \vec{S}_{ep}^2$. On the other hand, in case (1)

$$\tilde{F}_{PV} = \tilde{J} \vec{v}_{ep} \cdot \vec{S}_{ep}, \quad \tilde{F}_{PC} = \tilde{J} \vec{S}_{ep}^2, \quad (46)$$

$$\begin{aligned} \tilde{J} = & \int dE_1 \int dE_2 \delta(E_1 + E_2 - \epsilon_{ep}) \int_{-\pi}^{\pi} d\theta_1 |\sin \theta_1| \int_{-\pi}^{\pi} d\theta_2 |\sin \theta_2| p_1 p_2 U_0(x) W_0(y) \\ & \cdot \left(E_1 E_2 - p_1 p_2 (\cos(\theta_1 - \theta_2) - 2 \cos \theta_1 \cos \theta_2) - \delta_M \frac{m_1 m_2}{4} \right), \end{aligned} \quad (47)$$

where both $\vec{v}_{ep}, \vec{S}_{ep}$ are parallel to the first excitation axis $\propto \vec{k}_1$. The quantity \mathcal{R}_{ij} of eq.(13) is thus

$$\mathcal{R}_{ij} = (E_1 E_2 - p_1 p_2 (\cos(\theta_1 - \theta_2) - 2 \cos \theta_1 \cos \theta_2)) |b_{ij}^2| - \delta_M \frac{m_1 m_2}{4} \Re(b_{ij}^2). \quad (48)$$

RENP rates are numerically

$$\begin{aligned} \Gamma_{\text{RENP}} = & C |\vec{S}_{ep}|^2 |\chi|^2 \sum_{ij} \mathcal{F}_{ij} = 0.98 \times 10^{10} \text{ sec}^{-1} \text{ eV}^{-5} |\chi|^2 \frac{\sum_{ij} \mathcal{F}_{ij}}{\text{eV}^5} \\ & \times \frac{57.3 \text{ sec}^{-1}}{\gamma_{ep}} \frac{I_t}{10 \text{ mW cm}^{-2}} \left(\frac{R}{0.5 \text{ cm}} \right)^4 \left(\frac{L}{\text{cm}} \right)^2 \left(\frac{n}{1.4 \times 10^{19} \text{ cm}^{-3}} \right)^2. \end{aligned} \quad (49)$$

We compare results of improved computations given by \tilde{J} , based on direct plane-wave summation and approximate calculations, assuming the momentum conservation in Fig(7). There is a gap of vanishing contribution in an angular region for the approximate result due to that the momentum conservation gives a positive invariant squared mass to neutrino-pairs: $(K_0 - \omega_1 - \omega_2 + \omega_s)^2 - (\vec{K} - \vec{k}_1 - \vec{k}_2 + \vec{k}_s)^2 = (E_1 + E_2)^2 - (\vec{p}_1 + \vec{p}_2)^2 > 0$. Magnitudes of RENP rate are larger in improved computations by $O(10^4)$ and angular distributions are sharper than those in approximate results, as illustrated in Fig(7). It is dubious that this approximation is useful in experimental design, and it should be considered as a guide for more detailed computations based on more precise formulas.

Comparison of improved and approximate $\times 10^4$

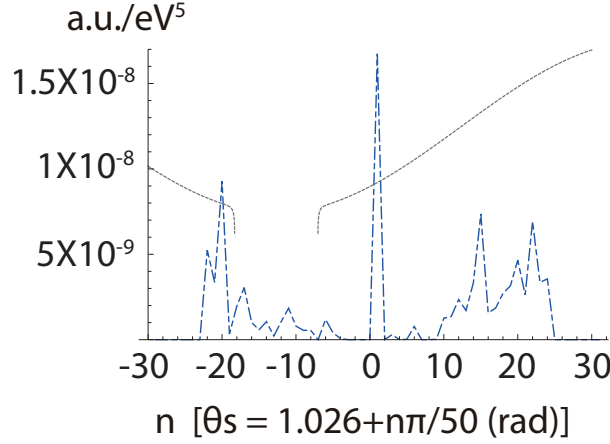


Figure 7: Comparison of approximate and improved RENP rate computations in case(1), taking heaviest neutrino pair of NH smallest mass 10 meV: precise result \tilde{J} in dash-dotted blue and approximate result $J \times 10^4$ in dotted black. A gap of vanishing contribution observed in the approximate result is due to the constraint of momentum conservation.

RENP rates for normal hierarchical (NH) mass pattern of smallest neutrino masses, 10 and 100 meV, are shown in Fig(8), which exhibit nearly, but not precisely, symmetrical angular distribution around $\theta_s = 1.026$ given by the degenerate triangle of $\vec{p}_i = 0$ among more general quadrangle vector relation of Fig(2). Angular distributions of rates are different in details for different neutrino masses, but Dirac and Majorana cases give the same distributions with magnitudes of typically 50% difference.

We turn again to parity violating magnetization. Amount of generated magnetization by neutrino pair emission is parity violating amplitude multiplied by magnetic moment in the state $|f\rangle$, hence its magnitude is

$$M = n\mu_B \langle f | \vec{L} + 2\vec{S} | f \rangle C |\chi|^2 \tilde{F}_{PV} = ng\mu_B \langle f | \vec{S} | f \rangle C |\chi|^2 \tilde{F}_{PV}. \quad (50)$$

We use g_{\perp} -factor of 5.9 for Er^{3+} in the first excited J-manifold ${}^4\text{I}_{13/2} \Gamma_{56}$ of trivalent Er ion [16]. The number density of Er ions in 0.1 % Er doped crystal (YLF) is $1.4 \times 10^{19} \text{cm}^{-3}$, which we shall use as a reference value. We further introduce a conversion factor to magnetic field from magnetic moment, ξ , since magnetization is measured outside the target, which gives $\mu_{\text{eff}} = \xi g\mu_B$ with

$$\mu_{\text{eff}} n = 0.29\text{G} \frac{\xi}{10^{-2}} \frac{n}{1.4 \times 10^{19} \text{cm}^{-3}}, \quad (51)$$

ξ is related to how near the target one measures magnetic field. To convert the generated magnetic moment $\vec{\mu}$ to the magnetic field caused by these moments, we use the formula of magnetic field due to magnetic moment $\vec{\mu}$,

$$\vec{B}(\vec{r}) = - \int d^3 r' n(\vec{r}') \left(\vec{\mu} \vec{\nabla}^2 \frac{1}{|\vec{r} - \vec{r}'|} - \vec{\nabla}(\vec{\mu} \cdot \vec{\nabla}) \frac{1}{|\vec{r} - \vec{r}'|} \right), \quad (52)$$

to be integrated over the target cylinder region ($n(\vec{r}')$ is the number density of RENP affected ions). When the measurement site is chosen to be close to the target region, the magnetic field generated by RENP may

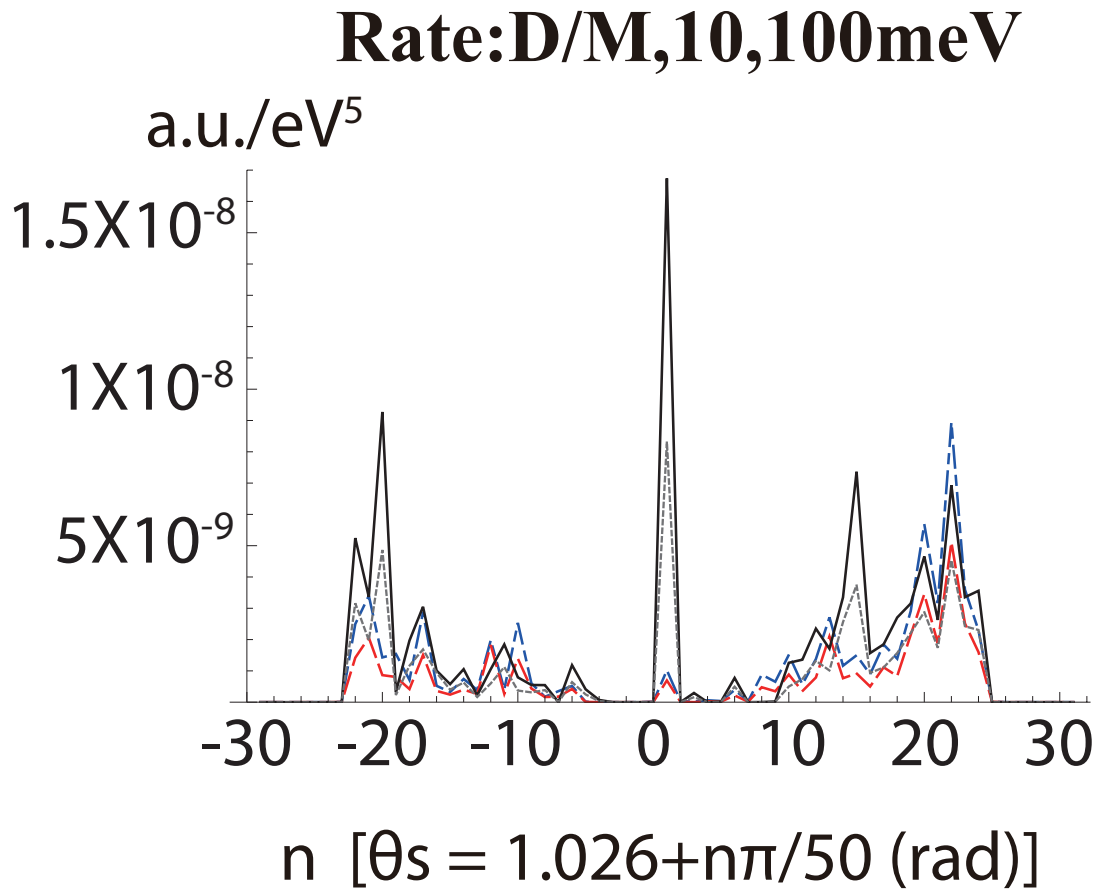


Figure 8: RENP rate angular distribution $\sum_{ij} \mathcal{F}_{ij}$ in eV⁵ unit: Dirac NH case of smallest mass 100 meV in joined black, Majorana NH 100 meV in dotted black, Dirac NH 10 meV in dash-dotted blue, and Majorana NH 10 meV in dashed red. Absolute rate is values times the number in eq.(49).

be effectively expressed as $\xi\mu n$, ξ being a fraction of RENP affected ions ≈ 0.01 for reference parameters. Actual value of ξ to be taken in magnetization depends on how experiment is done.

Magnetization generation rate in case (1) is given by

$$C|\chi|^2\xi\mu n\vec{S}_{ep}\cdot\vec{v}_{ep}\cos\theta_s\sum_{ij}\mathcal{G}_{ij},\quad\mathcal{G}_{ij}=\int dE_1\int dE_2\delta(E_1+E_2-\epsilon_{ep})\sqrt{E_1^2-m_i^2}\sqrt{E_2^2-m_j^2}$$

$$\cdot\int_{-\pi}^{\pi}d\theta_1\int_{-\pi}^{\pi}d\theta_2|\sin\theta_1\sin\theta_2|U_0\left(\frac{K_zL}{2}\right)W_0(K_{\perp}R)\mathcal{M}_{ij},\quad(53)$$

$$\mathcal{M}_{ij}=(E_1E_2-p_1p_2\cos(\theta_1-\theta_2)+2\cos\theta_1\cos\theta_2)2\Re(b_{ij}c_{ij}^*)-\delta_M\frac{m_im_j}{4}\Re(b_{ij}c_{ij}).\quad(54)$$

The angular cosine $\cos\theta_s$ arises from $\vec{k}\cdot\vec{S}_{ep}/k\propto\cos\theta_s$. Using $|\vec{v}_{ep}||\vec{S}_{ep}|=0.0157\times 2.49\times 10^{-6}/3.47=1.1\times 10^{-8}$, calculated magnetization at neutrino pair emission is numerically

$$2.1\times 10^3\text{G sec}^{-1}|\chi|^2\frac{\xi}{10^{-2}}\frac{I_t}{10\text{mWcm}^{-2}}\cos\theta_s\frac{\sum_{ij}\mathcal{G}_{ij}}{\text{eV}^5}\frac{\vec{S}_{ep}\cdot\vec{v}_{ep}}{|\vec{v}_{ep}||\vec{S}_{ep}|}\left(\frac{n}{1.4\times 10^{19}\text{cm}^{-3}}\right)^3\left(\frac{R}{0.5\text{cm}}\right)^4\left(\frac{L}{\text{cm}}\right)^2.\quad(55)$$

The number in front is for 57 msec of $1/\gamma_{ep}$, and if the value $\gamma_{ep}=2\pi\times 10$ MHz is taken, it is changed to 8×10^{-3} . A typical value for computed $\sum_{ij}\mathcal{G}_{ij}$ is of order 10^{-8}eV^5 , implying generated magnetization of order, $10^4|\chi|^2\text{nG sec}^{-1}$. See below on $|\chi|^2$.

We show a number of numerical results for case(1); the case of c-axis parallel to excitation laser wave vector \vec{k}_1 . Rate is proportional to $\mathcal{F}_{ij}\propto b_{ij}^2$, while magnetization is to $\cos\theta_s\mathcal{G}_{ij}\propto b_{ij}c_{ij}$, assuming CP conservation of all vanishing phase $\delta=\alpha=\beta=0$. Their angular distributions are illustrated in Fig(9) for four cases: NH (normal hierarchically ordered) cases of Dirac and Majorana neutrinos in the smallest mass of 10 and 100 meV. Different weights in rate and magnetization distributions in six neutrino-pair thresholds are calculable from neutrino oscillation data [17], and they are listed in the following table, assuming CP conservation case described by real number b_{ij}, c_{ij} . Fig(10) exhibits four dominant contributions of (11), (22), (12) and (33) pair thresholds. Individual pairs have different angular distributions of several peaks, which make the total sum complicated, but interesting. We have checked that Dirac/Majorana individual contributions differ in magnitudes, but not in peak positions and angular distributions.

We may summarize two important features of trivalent Er ion doped in YLF or similar host crystals;

(1) angular distributions for rate and magnetization have different structures dependent on different neutrino masses,

(2) Dirac/Majorana distinction appear only at quantitative level of absolute magnitudes.

(ij)	(11)	(12)	(22)	(13)	(23)	(33)
rate $\propto b_{ij}^2$	0.0311	0.405	0.0401	0.0325	0.0144	0.227
magnetization $\propto b_{ij}c_{ij}$	0.508	0.405	0.517	0.0325	0.0144	0.704

A good strategy for neutrino mass spectroscopy is to first determine the smallest neutrino mass irrespective of whether neutrinos are Dirac or Majorana particles, for instance by taking magnetization ratio of two largest peak regions. This way one can determine the smallest neutrino mass down to a level of order several to a few meV. The next step is to compare normalized magnetization magnitudes relative to its largest value of Majorana and Dirac cases, as illustrated in Fig(11). We illustrate thus normalized angular distributions at $\theta_s\geq 1.026$ for NH case of smallest neutrino mass 10 meV in Fig(11). The number of large peaks for magnetization may be defined by, say, $|\text{ratio}|>0.7$: we count that these are 3 for Dirac and 5 for Majorana from Fig(11). The threshold choice at 0.7 needs to be taken with care, and the method may not work for particular smallest neutrino masses. Even in this case a combined analysis may work. If one can unambiguously determine RENP rates at various signal photon directions, it can help the Majorana/Dirac distinction by using relative rate proportional to $\sum_{ij}\mathcal{F}_{ij}$ in conjunction with relative magnetization magnitude. The final step is thus to use both relative rate and magnetization for Majorana/Dirac distinction.

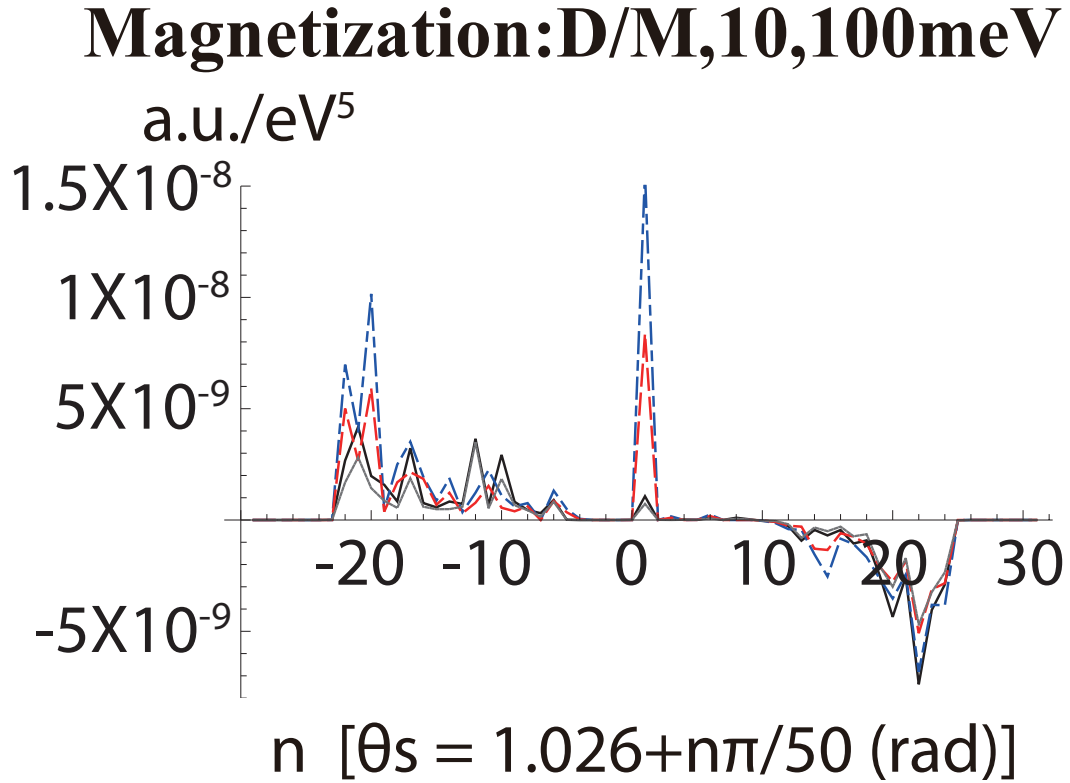


Figure 9: Magnetization angular distribution $\sum_{ij} \mathcal{G}_{ij}$ in eV⁵ unit: Dirac case of NH (normal hierarchically ordered) smallest mass 10 meV in joined solid black, and Majorana NH smallest mass 10 meV in joined dotted black, Dirac NH smallest mass 100 meV in dash-dotted blue, and Majorana NH smallest mass 100 meV in dashed red. (x-axis is $n = -30 \sim 30, \theta_s = 1.026 + n * \pi/50$.) Absolute value of generated magnetization rate is obtained by multiplying the number in eq.(55).

Indivisual pair contributions:(11),(12),(22),(33)

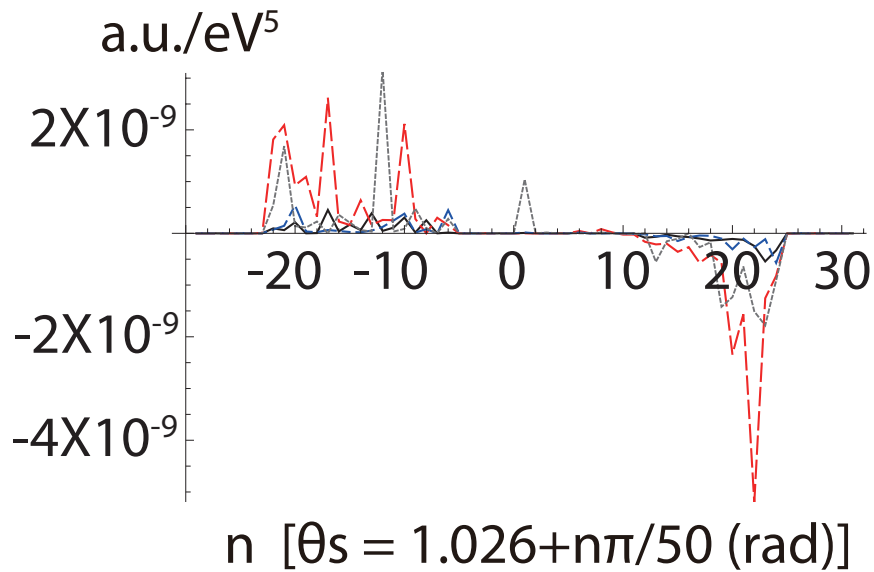
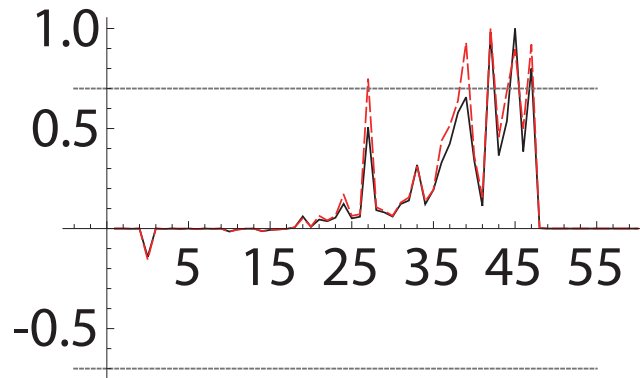


Figure 10: Magnetization angular distribution $\sum_{ij} \mathcal{G}_{ij}$ in eV^5 unit, taking Dirac NH case of smallest mass 10 meV: (11) contribution in solid black, (33) in dotted black, (22) in dash-dotted blue, and (12) in dashed red. Absolute rate is values times the number in eq.(49).

Large peaks ($|r| > 0.7$) for D/M: $m_1 = 10 \text{ meV}$

Ratio to max



n [$\theta_s = 1.026 + n\pi/100$ (rad)]

Figure 11: Large magnetization peak search for NH smallest mass 10 meV: Dirac case in solid black and Majorana case in dashed red. Ratio of maximum values with its absolute magnitudes > 0.7 is depicted in dotted black. x-axis value n is defined by angle $\theta_s = 1.026 + n\pi/100$.

Let us discuss the remaining important factor $|\chi|^2$. We assume CW (continuous wave) laser operation, and CW trigger laser is irradiated with a time lag after two-photon excitation. RENP events start to occur at trigger irradiation, and generated magnetization remains after events till spin relaxation time comes. Time evolution of population ρ_{ee} in the upper excited state $|e\rangle$ and coherence ρ_{ep} between levels of neutrino-pair emission is described by four-level optical Bloch equation, as given in Appendix. The coherence ρ_{eg} and population ρ_{ee} develop prior to trigger irradiation, and the coherence is partially transferred to ρ_{ep} after trigger irradiation. Time dependent $|\chi|^2$ is identified to be $|\rho_{ee}\rho_{ep}|^2$. Generation rates of magnetization are proportional to $n|\chi|^2 \propto \rho_{ee}^3|\rho_{ep}|^2$, which has a time structure, as illustrated in Fig(12). Note that event rate has a different power dependence $\rho_{ee}^2|\rho_{ep}|^2$. In our example of numerical computation, generated value $\rho_{ee}^3|\rho_{ep}|^2$ becomes of order, $10^{-2} \sim 10^{-3}$. It is important to note that this large value is realized for weak intensity I_1, I_2, I_t of three CW lasers, which however requires a small relaxation rate γ_{ep} . The largest RENP event occurs right after the trigger irradiation, accompanied by side events, which is somewhat similar to ringing phenomena of super-radiance events [2]. As stressed, signal of RENP events persists as magnetization till spin relaxation time, hence time-accumulated events show increasing profile of magnetization with time as in Fig(12). We confirmed that laser turn off leads to gradual decrease of $\rho_{ee}^3|\rho_{ep}|^2$. In actual experiments time-integrated magnetization till spin relaxation time is expected to be a readily observable quantity.

Generated and accumulated magnetization

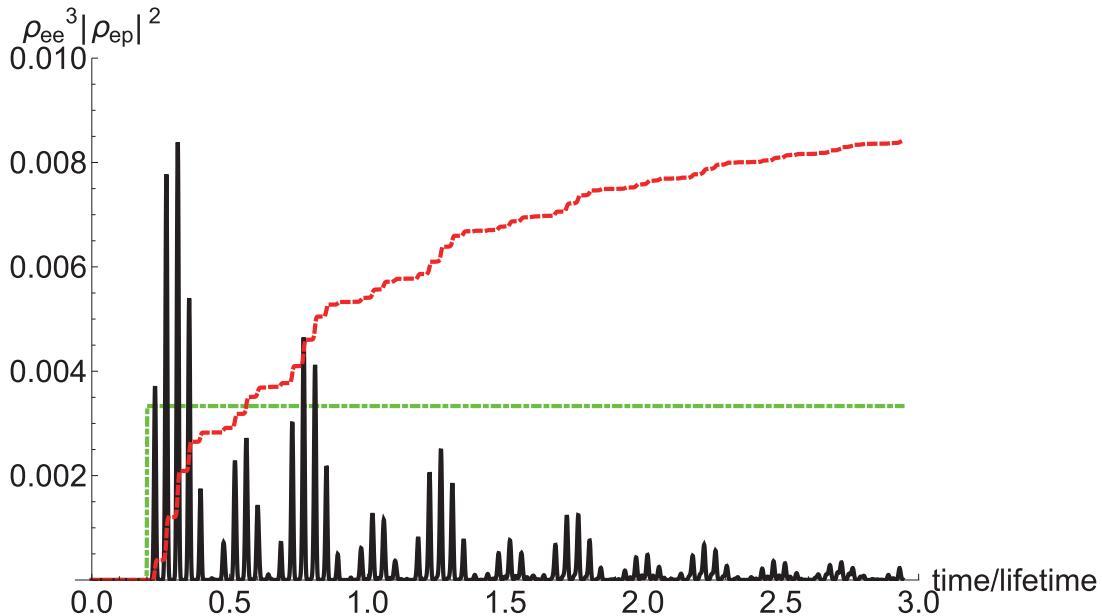


Figure 12: Time structure of magnetization generation rates $\propto \rho_{ee}^3|\rho_{ep}|^2$ (not to be confused with RENP event rate $\propto \rho_{ee}^2|\rho_{ep}|^2$) in solid black, when trigger is irradiated at $0.2 \times$ lifetime of state ${}^2\text{H}_{11/2}$ with time lag after irradiation of two-photon excitation lasers. Also shown is time profile of accumulated magnetization (ten times values of directly integrated result) in dashed red, which remain in crystals within this time scale. The same set of parameters as in Fig(13) is used here.

Our calculated magnetization rate per second is applicable at cycle end of three laser operation, and cycles are repeated with a cycle repetition time to taken ideally of order spin relaxation time. Thus, the quoted rate per second so far given should be multiplied by the number of repetition times per second. If the repetition cycle is 100 per second, the effective rate per second would be increased by 100. It would be

nice if one can make dedicated simulations including both spin relaxation and coherence development at the same time. For this simulation data of spin relaxation is needed. This is left to future works.

5 QED background

Major obstacle of QED background is the problem of extinction of initial ions in state $|e\rangle$ for RENP. Let us examine some details on features of potential QED backgrounds.

We first consider potentially dominant amplified QED event of two photon emission, $|e\rangle \rightarrow |g\rangle + \gamma_s + \gamma_b$ via $|p\rangle$, with extra background photon γ_b of energy ϵ_{ep} . Three vectors, $\vec{k}_1, \vec{k}_2, -\vec{k}_s$, are arranged to be in the same plane, hence four momentum vectors, $\vec{k}_1, \vec{k}_2, -\vec{k}_s, -\vec{k}_b$, form closed quadrangle to leading order of momentum conservation. One can directly prove that there is no extra photon vector \vec{k}_b satisfying the quadrangle relation, using parameter sets of proposed scheme. Still, the improved method of plane-wave summation in this work gives a finite contribution. Our estimate of finite size effect gives extinction rate per ion of order 3×10^{-4} , taking inhomogeneous width γ_e to be 1 MHz (effect $\propto \gamma_e^{-2}$). This rate is sufficiently small to ignore the process.

The next sub-dominant contribution is amplified three-photon emission, $|e\rangle \rightarrow |g\rangle + \gamma_s + \gamma_b + \gamma'_b$ with $\gamma_b + \gamma'_b = \epsilon_{ep}$. In order to suppress this process, we resort to symmetry and apply a weak magnetic field of order 100 G to distinguish by irradiated laser frequency two Zeeman states of separated doublet components. Zeeman split levels are given in terms of states of definite time reversal quantum numbers \pm ,

$$|J, \pm J_z\rangle = \frac{1}{\sqrt{2}}(|J, |J_z|, +\rangle \pm |J, |J_z|, -\rangle), \quad J_z > 0. \quad (56)$$

Optical transitions between two states of $|e\rangle, |p\rangle$ given by $|J, \pm J_z\rangle$ and $|J', \mp J'_z\rangle$, proceed via either single photon T-odd operator V_o or two-photon T-even operator V_e via paths of different energy, $|J, \pm J_z\rangle \rightarrow |J', \mp J'_z\rangle$ for T-odd case, $|J, \pm J_z\rangle \rightarrow |J', \pm J'_z\rangle$ for T-even case. This situation occurs due to cancellation of two terms, for instance between $|J, |J_z|, \pm\rangle \rightarrow |J', |J'_z|, \pm\rangle$ for T-odd case. One can thus single out T-odd transition by laser frequency, rejecting two photon emission. On the other hand, when Kramers degeneracy exists in the zero field, both T-even and T-odd transitions occur since lasers cannot distinguish two modes of transitions.

This leaves amplified four-photon emission, $|e\rangle \rightarrow |g\rangle + \gamma_s + \gamma_1 + \gamma_2 + \gamma_3$, of QED origin as the main extinction process. Estimate of total rate of this process is as follows. Except a common factor related to signal photon part, the major difference arises from coupling factors and phase space integration either over two-body or three-body states. Coupling factors of QED background is of order, $(\text{dipole}^2/3)^3 \approx 10^{-39} \text{eV}^{-6}$, while RENP coupling is of order $G_F^2 \approx 10^{-46} \text{eV}^{-4}$. Three-body phase space of background QED photons have

$$\left(\frac{2}{3}\right)^3 \int \frac{d\omega_1 d\omega_2 d\omega_3}{(2\pi)^5} \delta\left(\sum_i \omega_i - \epsilon_{ep}\right) \frac{\omega_1^3 \omega_2^3 \omega_3^3}{\Delta_1^2 \Delta_2^2} = \left(\frac{2}{3}\right)^3 \frac{\epsilon_{ep}^{11}}{(2\pi)^5 \bar{\Delta}_1^2 \bar{\Delta}_2^2} \frac{1}{184800},$$

where energy denominators $\Delta_i, i = 1, 2$ that appear in perturbation theory are linear combinations of level energy differences ϵ_{ab} and one of emitted photon energies $\omega_i, i = 1, 2, 3$, with $\bar{\Delta}_i$ its appropriate average value, while two-neutrino phase space has

$$(4\pi)^2 \int \frac{dE_1 dE_2}{(2\pi)^5} \delta\left(\sum_i E_i - \epsilon_{ep}\right) = \frac{2}{15(2\pi)^3} \epsilon_{ep}^5.$$

Thus, the ratio of three- to two-body phase space is of order, $3 \times 10^{-7} (\epsilon_{ep}^6 / \bar{\Delta}_1^2 \bar{\Delta}_2^2)$, which gives roughly comparable magnitude of amplified QED background to RENP events. Even if the four-photon process depletes to some extent the excited state $|e\rangle$, parity violating magnetization can single out RENP process.

Finally, we mention parity violating magnetization caused by spontaneous emission from state $|e\rangle$ to the strongest ground J-manifold. Single photon emission to states of different T quantum number is allowed,

and there are eight of them in the lowest J-manifold, ${}^4I_{15/2}$, since eight Stark levels are degenerate under time reversal. But this is not a problem, because magnetization measurement due to RENP effectively ends a cycle at lifetime of this state, and cycles are repeated again.

6 Summary and Outlook

Even if the experimentally confirmed macro-coherence amplification works, the major problem for a successful RENP measurement of process $|e\rangle \rightarrow |g\rangle + \gamma_s + \nu\bar{\nu}$ is how to reject similarly amplified QED backgrounds. We proposed in this paper a method of overcoming this difficulty by measuring parity violating observable present in weak interaction and absent in QED. The proposed magnetization along the signal photon direction is parity violating, and emerges with reasonably large magnitudes, if one adopts a clever way of choosing excitation and trigger directions and their photon energies. The best candidate target we have found so far is trivalent lanthanoid ion of odd number of 4f electrons: Er^{3+} doped in host crystals such as YLF. Host crystals should provide to the ion a sharp radiative width and a large spin relaxation time. Moreover, the Kramers degeneracy of odd number 4f systems such as Er^{3+} brings about an experimental bonus. Excitation at $|g\rangle \rightarrow |e\rangle$ is done by T(time reversal)-even two-photon process to imprint a phase to target ions, while macro-coherence generation between states of neutrino pair emission is achieved via single photon T-odd trigger laser irradiation with a time lag. Numerical simulations using four-level optical Bloch equation supports a sizable generation of coherence and population among relevant states.

Calculation of magnetization suffers from uncertainty, most notably due to a lack of optical experimental data of separated magnetic and electric dipole transitions between two relevant states of neutrino pair emission. Generated magnetization may however become of order 10^2 nG sec^{-1} for 0.1% concentration of trivalent Er ion. Crystal field of surrounding host ions introduces an environmental parity violation, a necessary ingredient for a successful measurement of RENP originated magnetization. Numerical analysis of RENP rate and magnetization have been accomplished by incorporating finite size effect of target crystal, which is important due to realistic crystal sizes of order 1 cm used in experiments.

Angular distribution of magnetization has a good sensitivity to the smallest neutrino mass down to a few to several meV. Majorana/Dirac distinction is made possible by elaborate analysis combined with direct RENP event rates. Although we did not study sensitivity to CP violation parameters, it is expected to be good.

A rich variety of angular structures resulting from incorporation of finite size effect as seen in Fig(8) and Fig(9) is not really what we can measure in actual experiments, since detector angular resolutions, in particular for magnetization measurement using SQUID, should be considered. We may expect to observe smoothed out distributions, but details of the smooth-out should be worked out taking into account angular resolution of adopted detector. It is rather better to first set up experimental goals for neutrino parameters, and to design and choose detector system matching this objective by detailed simulations using the method developed in the present work. In the meantime it is desirable to measure electric and magnetic dipole transition rates between two relevant ion states in crystals such as $\text{Er}^{3+}:\text{YLF}$.

7 Appendix: Optical Bloch equation for estimate of population and coherence

Before we present four-level optical Bloch equation and its numerical simulations, we give an intuitive picture of what may be realized in ideal situations. Suppose that trigger laser irradiation is followed by two-laser excitation after a time lag. All lasers are assumed to be operated by CW (continuous wave) mode, which effectively means that lasers are irradiated during the entire lifetime scale. One may take Rabi frequencies much larger than radiative decay rates, $\Omega_{ab} = \sqrt{d_{ab}^2 + \mu_{ab}^2} E \gg \gamma_{ab}$, using a reasonable range of laser intensity, $I_t = E^2 = B^2$.

CW steady state solution derived by analysis of ladder-type three-level optical Bloch equation after various lifetimes has the following form of population and coherence, in the zero detuning limit, [18], [19],

$$\begin{pmatrix} \rho_{ee} \\ \rho_{gg} \\ \rho_{qq} \\ \rho_{eg} \\ \rho_{eq} \\ \rho_{qg} \end{pmatrix}_0 = \frac{1}{\Omega_{eq}^2 + \Omega_{qg}^2} \begin{pmatrix} \Omega_{qg}^2 \\ \Omega_{eq}^2 \\ 0 \\ -\Omega_{eq}\Omega_{qg} \\ 0 \\ 0 \end{pmatrix} + O(\gamma_{ab}). \quad (57)$$

It is thus possible to generate a maximal coherence, $|\rho_{eg}| = 1/2$ between $|e\rangle$ and $|g\rangle$, with population ratio of 1 : 1 : 0 between three levels $|e\rangle, |g\rangle, |q\rangle$ when $\Omega_{qg} = \Omega_{eq}$. A nearly complete inverted population to $|e\rangle$ is also possible when $\Omega_{qg} \gg \Omega_{eq}$, the inequality sometimes felt counter-intuitive.

Suppose that trigger laser matched to energy difference of $|g\rangle$ and $|p\rangle$ is irradiated with a time lag when the steady state caused by two-photon excitation is being formed. One can then effectively consider three level V-scheme in which two lasers irradiated between $|g\rangle, |e\rangle$ are replaced by an effective single laser, forming V-type laser irradiation along with trigger $|g\rangle \rightarrow |p\rangle$. The steady-state solution of V-type is given by [19]

$$\begin{pmatrix} \rho_{ee} \\ \rho_{gg} \\ \rho_{pp} \\ \rho_{eg} \\ \rho_{ep} \\ \rho_{pg} \end{pmatrix} = \frac{1}{2(\Omega_{eg}^2 + \Omega_{pg}^2)} \begin{pmatrix} \Omega_{eg}^2 \\ \Omega_{eg}^2 + \Omega_{pg}^2 \\ \Omega_{pg}^2 \\ 0 \\ \Omega_{eg}\Omega_{pg} \\ 0 \end{pmatrix} + O(\gamma_{ab}). \quad (58)$$

One can thus generate a large coherence between states, $|p\rangle, |e\rangle$, provided that Rabi frequencies, an effective Ω_{eg} and Ω_{pg} , are of comparable magnitudes. For instance, $\rho_{ep} = 1/4$ for $\Omega_{pg} = \Omega_{eg}$. This is important, because neutrino pairs are emitted between these states and large coherence is required for ρ_{ep} .

The picture here is a kind of coherence transfer from ρ_{eg} at excitation to ρ_{ep} at trigger. We would like to check whether this picture is realized in four-level problem under three laser excitation advocated in the text.

The four-level optical Bloch equation of our interest concerns 16 component vector $\vec{\sigma}_4$, and is given by a set of linear differential equations [20],

$$\frac{d}{dt} \vec{\sigma}_4 = \mathcal{R}_4 \vec{\sigma}_4, \quad (59)$$

$$\vec{\sigma}_4^T = (\rho_{ee}, \rho_{gg}, \rho_{qq}, \rho_{pp}, e^{-i(\delta_{eq} + \delta_{qg} + \delta_{pg})t} \rho_{ge}, e^{i(\delta_{eq} + \delta_{qg} + \delta_{pg})t} \rho_{eg}, e^{-i\delta_{eq}t} \rho_{qe}, e^{i\delta_{eq}t} \rho_{eq}, e^{i\delta_{qg}t} \rho_{qg}, e^{-i\delta_{qg}t} \rho_{gq}, e^{i\delta_{pg}t} \rho_{pg}, e^{-i\delta_{pg}t} \rho_{gp}, \rho_{pe}, \rho_{ep}, \rho_{pq}, \rho_{qp}), \quad (60)$$

where 16×16 \mathcal{R}_4 matrix has the following form in the case of no de-tuning of $\delta_{ab} = 0$,

$$\mathcal{R}_4 = \begin{pmatrix} A & C_1 & C_2 \\ D_1 & B_1 & E \\ D_2 & F & B_2 \end{pmatrix}, \quad (61)$$

$$A = \begin{pmatrix} -\gamma_{eg} - \gamma_{eq} - \gamma_{ep} & 0 & 0 & 0 \\ \gamma_{eg} & 0 & \gamma_{qg} & \gamma_{pg} \\ \gamma_{eq} & 0 & -\gamma_{qg} - \gamma_{qp} & 0 \\ \gamma_{ep} & 0 & \gamma_{qp} & -\gamma_{pg} \end{pmatrix}, \quad (62)$$

$$B_1 = \frac{1}{2} \begin{pmatrix} -\Gamma_{eg} & 0 & -i\Omega_{qg} & 0 & 0 & i\Omega_{eq} \\ 0 & -\Gamma_{eg} & 0 & i\Omega_{qg} & -i\Omega_{eq} & 0 \\ -i\Omega_{qg} & 0 & -\Gamma_{eq} & 0 & 0 & 0 \\ 0 & i\Omega_{qg} & 0 & -\Gamma_{eq} & 0 & 0 \\ 0 & -i\Omega_{eq} & 0 & 0 & -\Gamma_{qg} & 0 \\ i\Omega_{eq} & 0 & 0 & 0 & 0 & -\Gamma_{qg} \end{pmatrix}, \quad (63)$$

$$B_2 = \frac{1}{2} \begin{pmatrix} -\Gamma_{pg} & 0 & 0 & 0 & i\Omega_{qg} & 0 \\ 0 & -\Gamma_{pg} & 0 & 0 & 0 & -i\Omega_{qg} \\ 0 & 0 & -\Gamma_{ep} & 0 & i\Omega_{eq} & 0 \\ 0 & 0 & 0 & -\Gamma_{ep} & 0 & -i\Omega_{eq} \\ i\Omega_{qg} & 0 & i\Omega_{eq} & 0 & -\Gamma_{pq} & 0 \\ 0 & -i\Omega_{qg} & 0 & -i\Omega_{eq} & 0 & -\Gamma_{pq} \end{pmatrix}, \quad (64)$$

$$C_1 = D_1^T = \frac{1}{2} \begin{pmatrix} 0 & 0 & i\Omega_{eq} & -i\Omega_{eq} & 0 & 0 \\ 0 & 0 & 0 & 0 & i\Omega_{qg} & -i\Omega_{qg} \\ 0 & 0 & -i\Omega_{eq} & i\Omega_{eq} & -i\Omega_{qg} & i\Omega_{qg} \\ 0 & 0 & 0 & 0 & 0 & 0 \end{pmatrix}, \quad (65)$$

$$C_2 = D_2^T = \frac{1}{2} \begin{pmatrix} 0 & 0 & 0 & 0 & 0 & 0 \\ -i\Omega_{pg} & i\Omega_{pg} & 0 & 0 & 0 & 0 \\ 0 & 0 & 0 & 0 & 0 & 0 \\ i\Omega_{pg} & -i\Omega_{pg} & 0 & 0 & 0 & 0 \end{pmatrix}, \quad (66)$$

$$E = F^T = \frac{1}{2} \begin{pmatrix} 0 & 0 & -i\Omega_{pg} & 0 & 0 & 0 \\ 0 & 0 & 0 & i\Omega_{pg} & 0 & 0 \\ 0 & 0 & 0 & 0 & 0 & 0 \\ 0 & 0 & 0 & 0 & 0 & 0 \\ 0 & 0 & 0 & 0 & 0 & i\Omega_{pg} \\ 0 & 0 & 0 & 0 & -i\Omega_{pg} & 0 \end{pmatrix}, \quad (67)$$

$$\Gamma_{eg} = \gamma_{eg} + \gamma_{eq} + \gamma_{ep}, \quad \Gamma_{eq} = \Gamma_{eg} + \gamma_{qp} + \gamma_{qg}, \quad \Gamma_{qg} = \gamma_{qp} + \gamma_{qg}, \quad (68)$$

$$\Gamma_{pg} = \gamma_{pg}, \quad \Gamma_{ep} = \Gamma_{eg} + \gamma_{pg}, \quad \Gamma_{pq} = \Gamma_{qg} + \gamma_{pg}. \quad (69)$$

We are bound to use for relaxation radiative decay rates due to lack of inhomogeneous widths in actual host crystals. This might be a proper choice when we use lowest Stark levels, but experimental data of relaxation rates of lowest Stark states in each J-manifold are needed to settle this question. Time unit used in simulations is the lifetime 1.7 msec of $|e\rangle = \text{Er}^{3+} {}^2\text{H}_{11/2}$. Calculated Rabi frequencies $\Omega_{ab} = d_{ab}E = 2\pi\nu_{ab}$ under CW operation of powers $\sim 10\text{mWcm}^{-2} = 1.26 \times 10^{-3}\text{eV}^2$ are of orders,

$$\nu_{pg} = 174\text{kHz}\sqrt{\frac{I_t}{10\text{mWcm}^{-2}}}, \quad \nu_{qg} = 37.4\text{kHz}\sqrt{\frac{I_t}{10\text{mWcm}^{-2}}}, \quad \nu_{eq} = 20.9\text{kHz}\sqrt{\frac{I_t}{10\text{mWcm}^{-2}}}, \quad (70)$$

using calculated A-coefficients in the text. Divided by respective radiative decay rates, these Ω/γ are $(4.0, 5.1, 4.0) \times 10^4 \sqrt{\frac{I_t}{10\text{mWcm}^{-2}}}$. Computation of Fig(13) corresponds to use of CW laser power of order $\mu\text{W cm}^{-2}$ or less during a few msec irradiation.

Solution of large coherence ρ_{ep} generation is illustrated in Fig(13), which shows a kind of coherence transfer at the trigger irradiation, as suggested by heuristic argument using three-level optical Bloch equation. Thus, there are ranges of laser parameter that give rise to sufficiently large coherence and population.

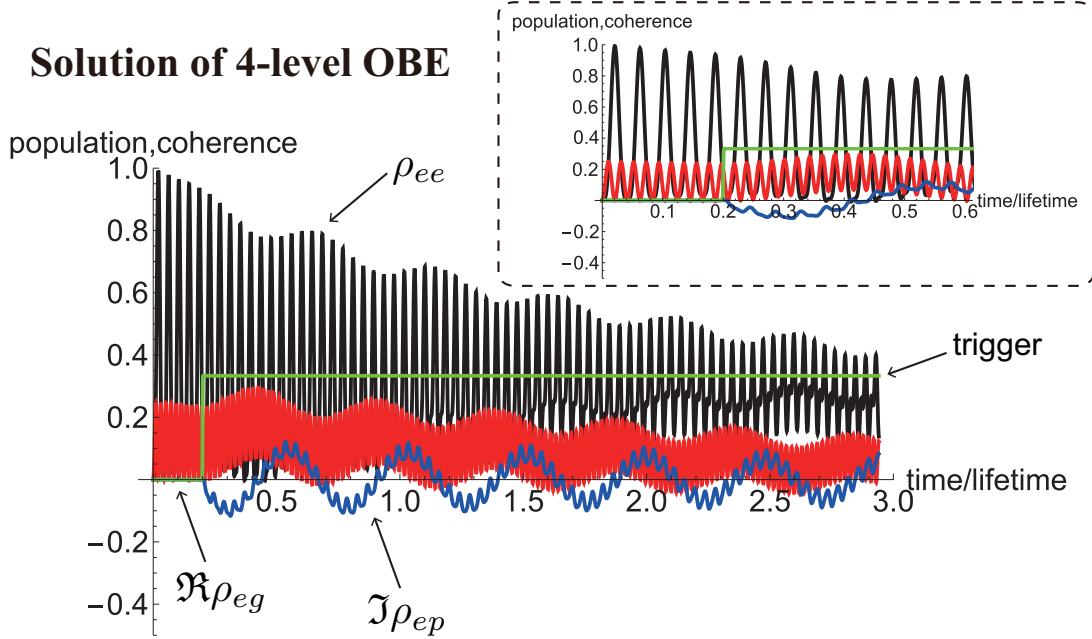


Figure 13: Solution of four-level optical Bloch equation under CW trigger with a time lag: ρ_{ee} in black, $\Re\rho_{eg}$ ($\Im\rho_{eg} \ll \Re\rho_{eg}$) in red, and $\Im\rho_{ep}$ ($\Re\rho_{ep} \ll \Im\rho_{ep}$) in blue. For reference the trigger profile with time lag is shown in green. Coherence transfer from ρ_{eg} in red to ρ_{ep} in blue is observed at the time of trigger irradiation. Assumed laser intensities are $I_{qg} = 3\text{mW cm}^{-2}$, $I_{eq} = 9\text{mW cm}^{-2}$, $I_{pg} = 1\mu\text{W cm}^{-2}$.

RENp magnetization emerges with time profile as illustrated in Fig(12) of the text, since rates are proportional to $\rho_{ee}^3|\rho_{ep}|^2$.

Acknowledgements

This research was partially supported by Grant-in-Aid 21H01112(HH), 20H00161(AY), and 17H02895 (MY) from the Ministry of Education, Culture, Sports, Science, and Technology.

References

- [1] A. Fukumi et al., Prog. Theor. Exp. Phys. (2012) 04D002, and references therein.
- [2] R.H. Dicke, Phys.Rev. **93**, 99 (1954).
For a review, M.G. Benedict, A.M. Ermolaev, V.A. Malyshev, I.V. Sokolov, and E.D. Trifonov, *Super-radiance - Multiatomic coherent emission -*, informa (New York), 1996.
- [3] Y. Miyamoto et al., PTEP, 113C01 (2014).
Y. Miyamoto et al., PTEP, 081C01 (2015).
T. Hiraki et al., J. Phys. B: At. Mol. Opt. Phys. **52** 045401 (2019).

- [4] H. Hara and M. Yoshimura, Eur.Phys.J. **C79** 684(2019), and arXiv: 1904.03813v1 (2019).
- [5] M. Yoshimura, N. Sasao, and S. Uetake, Phys.Rev.**D 90**, 013022 (2014).
- [6] A preliminary version of the scheme was presented in an invited talk at workshop on " Determination of the effective electron neutrino mass" at ECT*, Trento, Italy, February 11 (2020). See also *Persistent magnetization at neutrino pair emission* , M. Yoshimura, arXiv: 2004.03812v1[hep-ph] (2020).
- [7] J.H. Van Vleck, J. Chem. Phys. **41**, 67 (1937).
- [8] B.R. Judd, Phys.Rev.**127**, 750(1962). G.S. Ofelt, J. Chem. Phys. **37**, 511 (1961).
- [9] M. Yoshimura, Phys. Rev. **D75**, 113007(2007).
- [10] Even number of 4f electron systems may also become candidates if host crystals allow symmetry to produce time reversal degeneracy. For instance, the ground Stark state of trivalent Ho($4f^{10}$) in YLF is a $T = \pm$ doublet of symmetry S_4 . Two lowest Stark singlets of $T = +$ and $T = -$ in upper J-manifolds may be used for RENP scheme in much the same way as in trivalent Er.
- [11] A good overview of lanthanoid ion spectroscopy is given in B.G. Wybourne, *Spectroscopic properties of rare earths*, John Wiley and Sons, (1965).
- [12] P.A. Loiko et al., J. Luminescence, **185** , 279 (2017).
- [13] In the literature such as I.I. Sobelman, *Atomic Spectra and Radiative Transitions*, 2nd edition, Springer (1991), there are extensive discussion on $2s \rightarrow 1s$ transitions in high Z hydrogen-like atoms, namely competition of two-photon and magnetic dipole single-photon decays. When LS coupling scheme holds for small Z, the magnetic dipole transition is forbidden, which explains why two-photon emission dominates over magnetic dipole emission in pure hydrogen. What is compared however involves spin degrees of freedom, T-even two-photon emission of no spin-flip, $2s \uparrow \rightarrow 1s \uparrow$, and T-odd magnetic dipole emission of spin-flip, $2s \uparrow \rightarrow 1s \downarrow$. Hence, the hydrogen-like problem of competitive two-photon and single-photon processes is not applicable in our problem.
- [14] D. Aberg and S. Edvardsson, Phys. Rev. **B65**, 045111 (2002).
- [15] We correct a sign mistake of h_2 in pair emission amplitudes given in the literature [9], eq.(20) and eq.(21).
- [16] Due to lack of data for our adopted host crystal, we take g-factors of Er:YLF given in K.I. Gerasimov et al, Phys.Rev. **B 94**, 054429 (2016).
- [17] For a review of neutrino oscillation experiments, Particle Data Group Collaboration, M. Tanabashi et al., Phys. Rev. D 98 030001 (2018).
- [18] Y.B. Band, *Light and Matter*, Wiley (2006).
- [19] T. Takahashi and M. Yoshimura, Unpublished note, "Enhanced Weak Rate under Cyclic Atomic Transition", (June, 2007).
- [20] A general form of optical Bloch equation was first given by G. Lindblad, *Commun. math. Phys.***48**, 119(1976).